Dynamic Loading of Polycrystalline Shape Memory Alloy Rods

Peter Popov [a] K. Ravi-Chandar [b] Khalid Sarh [c]
Dimitris C. Lagoudas [a,*]

[a] *Department Of Aerospace Engineering, Texas A&M University, TX 77843-3141, USA*

[b] *Department of Aerospace Engineering and Engineering Mechanics, University of Texas at Austin, Austin, TX 78712-1085, USA*

[c] *Department of Mechanical Engineering, University of Houston, TX 77204-4792, USA*

Abstract

Shape Memory Alloys (SMA) have recently been considered for applications where dynamic loading is applied. An SMA body subjected to external dynamic loading will experience large inelastic deformations that will propagate through the body as phase transformation fronts. The wave propagation in a cylindrical SMA rod induced by an impact loading is considered. Some applications of this model problem include energy absorbing and vibration damping devices. The constitutive model being used is the one by Lagoudas, Bo and Qidwai. The problem is solved numerically by an adaptive Finite Element Method (FEM) based on the Zienkiewicz-Zhu error estimator. A model problem featuring a fixed impact stress load propagating through the rod is solved and compared to known analytical solutions. The energy dissipation capabilities of SMA materials are investigated for a square pulse model problem at various operational temperatures. We then present experimental results for wave propagation in SMA rods. A Hopkinson bar apparatus is used to make a uniaxial test of a NiTi specimen. Strain history records by strain gauges placed at different locations along the SMA rod are compared with numerical calculations using the adaptive FEM technique.

Key words: Shape Memory Alloy, Dynamic Analysis, Adaptive FEM,Hopkinson Bar

* Corresponding author.
Email addresses: ppopov@tamu.edu (Peter Popov), kravi@mail.utexas.edu (K. Ravi-Chandar), lagoudas@aero.tamu.edu (Dimitris C. Lagoudas).

1 Introduction

There are many areas of application which can successfully utilize the unique properties of SMAs. The research presented in this paper relates directly to the design of SMA components capable of absorbing dynamic loads. Such components can be integrated into critical parts of structures that may need protection from impact loads. Examples include joints that connect the hull of an underwater vehicle with its internal structure, tank armor, cargo containers, etc. Another promising field of applications includes various active or passive vibration damping devices. Many different devices have been proposed among which SMA elements (Yiu and Regelbrugge, 1995; Graesser, 1995), wires (Thomson et al., 1995; Fosdick and Ketema, 1998) or rods (Feng and Li, 1996). In a recent paper (Lagoudas et al., 2001) the authors investigate numerically the vibration damping capabilities of generic SMA components. A related study (Mayes and Lagoudas, 2001) demonstrates experimentally the feasibility of devices composed of NiTi SMA tubes.

Shape Memory Alloys are a class of materials that change their internal structure due to changes in temperature and/or externally applied loads. At high temperatures and low stress levels the crystal lattice is in the high symmetry austenite phase (A). At low temperatures or high stress levels the material exists in a low symmetry martensite phase (M). The phase transition is diffusionless and is characterized by shear deformations of entire regions inside the material (Wayman, 1983). What makes SMA materials remarkably different from ordinary metals is the *shape memory effect* and the effect of *pseudoelasticity* which are associated with the specific way the phase transition occurs (Funakubo, 1987). The *shape memory effect* allows material which has been deformed while in the martensitic phase to recover its shape upon heating. The mechanism behind this behavior is the ability of SMAs to allow detwinning of the self-accomodated martensitic variants. The *pseudelasticity* in SMA is their ability to support large recoverable inelastic strains. The primary way in which such strains are created is the stress induced phase transition from austenite to martensite. The deformations are recovered upon unloading. The pseudoelastic response provides both energy dissipation capabilities and shape recovery while utilizing the shape memory effect leads to dissipation of mechanical energy but the SMA component/structure has to be then reheated to recover its shape.

Several constitutive models have been developed in recent years to model the shape memory effect and pseudoelasticity of polycrystalline SMAs. Among the most widely accepted rate independent models are the exponential (Tanaka, 1986), cosine (Liang and Rogers, 1990) and polynomial (Boyd and Lagoudas, 1996). Any of these models can be unified in the framework of a constitutive model (Lagoudas et al., 1996; Boyd and Lagoudas, 1994) based on the selec-

tion of appropriate thermodynamic potentials. It has been shown there that these three models can be obtained by specific selection for the form of the Gibbs free energy. The constitutive model is extended in (Bo and Lagoudas, 1999a,b,c,d) to incorporate plastic deformations and to account for the evolution of the internal state variables during cyclic loading. In the model proposed by (Brinson, 1993; Brinson and Lammering, 1993) the martensitic volume fraction is subdivided in two parts to account for thermally and stress induced phase transformation. A different approach is taken in (Abeyaratne et al., 1993, 1994; Abeyaratne and Knowles, 1993) where the possibility for softening during phase transformation is considered. The model is rate dependent and the hysteresis is modelled by an N shaped trilinear stress-strain curve. Other authors such as (Patoor et al., 1996; Siderey et al., 1999; Sun and Hwang, 1993a,b) use micromechanical techniques to average the response of single crystal martensitic variants and obtain a model for the macroscopic behavior of polycrystalline SMAs. For further details on SMA models the reader is referred to the review paper (Birman, 1996). In this paper we chose to use the unified approach (Lagoudas et al., 1996), which can accommodate the rate independent constitutive models for SMAs.

Classical rate-independent plasticity theory is not sufficient to describe the behavior of SMA materials. While it cannot model properly the pseudoelastic response it is still capable of partially [1] predicting the shape memory effect. Theoretical developments on elasto-plastic wave propagation in long slender rods dates back to the works of Von Karman (1942), Rakhmatulin (1945) and Taylor (1958). Extensive experiments on elasto-plastic wave propagation have been carried out by Bell (1962); Chiddister and Malvern (1963); Kolsky (1949); Clifton and Bodner (1966); Bodner and Clifton (1967) using a split-Hopkinson bar apparatus. The technique itself was introduced by Kolsky (1949). The reader is referred to classical texts on wave propagation such as (Kolsky, 1963; Graff, 1975) for additional information. In recent years there have been extensions to the Hopkinson technique (Nemat-Nasser et al., 1991) that allow for dynamic test recovery in both tension and compression.

Abeyaratne and Knowles (1991) studied the dynamics of phase transformation in piecewise linear elastic materials with non-monotone hysteresis. A unique solution was obtained with the use of a kinetic relation controlling the rate of the phase transformation together with a nucleation condition for the initiation of the transformation to render a unique. The same authors extended their analysis in (Abeyaratne and Knowles, 1994a,b) to account for thermal effects. In a general setting Pence (1986) considered wave propagating in a nonlinear elastic bar with a non-monotonic stress-strain relationship subjected to a monotonically increasing load. It was found that for sufficiently high loads a strain discontinuity associated with phase transformation is being created.

[1] without the strain recovery upon heating

In a recent paper (Chen and Lagoudas, 2000) the rate independent model for polycrystalline SMAs (Lagoudas et al., 1996) is employed to obtain solutions to the coupled thermomechanical problem for SMA materials with monotone hardening behavior. The authors take into account the latent heat generation and assuming adiabatic conditions they solve the problem by the method of characteristics together with jump conditions that yield unique solutions. A similar study (Bekker et al., 2002), but for different constitutive models (linear and cubic) has been carried out for both isothermal and adiabatic conditions.

The complex nature of most constitutive laws for SMA materials however makes direct integration of even the simplest uniaxial transient initial boundary value problems (IBVP) very complicated. Closed form solutions can usually be obtained if certain simplifications in the model being used are assumed e.g. constant material properties independent of the amount of phase transformation (Bekker et al., 2002). Numerical attempts to solve this problem usually employ Finite Difference (FD) schemes. Extensive numerical treatment of the shock loading problem for SMA rods by finite difference scheme has been done by (Jimenez-Vicktory, 1999). In this study it was shown that explicit FD schemes either introduce too much numerical dissipation which pollutes the solution or artificial viscosity techniques have to be used in order to remove oscillations near shock discontinuities in the numerical solution. In a different setting, (Oberaigner et al., 1996) investigates numerically the coupled problem of wave propagation and heat transfer in an SMA rod. The authors focus on stress pulses of low magnitude that causes only elastic deformations. The temperature at one end of the SMA rod is chosen dynamically in a such a way as to utilize the phase change due to the shape memory effect in order to maximize the damping of the rod.

There has been limited amount of experimental work done on characterizing the dynamic response of SMAs. An experimental study on the propagation of shear waves in single crystal Cu-Al-Ni shape memory alloy has been done in (Escobar and Clifton, 1993). Phase transition shock were not observed directly due to their low propagation speed. Instead, their presence is inferred from the measurements of the elastic waves at the rear end of the specimen. An analytical attempt to model these experiments is presented in Abeyaratne and Knowles (1997).

The main focus of this paper is the the one-dimensional dynamic problem of loading an SMA rod under conditions of pseudoelasticity and shape memory effect. We present an experiment on the wave propagation in a NiTi SMA rod performed in a Hopkinson bar apparatus. The results are compared with a FEM computational simulation. We utilize adaptive meshing techniques based on the Zienkiewicz-Zhu error estimator (Zienkiewicz, 1987) in order to improve the accuracy of the method and decrease computational time. The pseudoelastic effect in SMAs can be activated after special conditioning, e.g.

marformung. Without such preparation specimens will exhibit either simple plastic or/and detwinning transformations. There are substantial difficulties in properly conditioning long NiTi rods in order to activate the pseudoelastic effect. In addition there are also problems configuring an experimental setup in order to test at elevated temperatures required to have pseudoelastic response. The experiment presented in this paper is done under detwinning conditions.

We begin the discussion with a brief overview in Section 2 of the constitutive laws, field equations and boundary conditions defining our problem. Then, in Section 3.1 we outline the implementation of the FEM for the NiTi SMA. The adaptive strategy is presented in Section 3.2. In order to verify the implementation of the adaptive FEM in Section 4.1 we solve a boundary value problem with a step-function boundary condition for which there are existing analytical solutions in the literature. Then, in Section 4.2 we study a square pulse model for two different thermomechanical paths and give expected values for energy dissipation as the pulse propagates through the rod. Section 5 describes the Hopkinson bar experiment and discusses the dynamic characterization of SMA materials. Finally, in Section 6 we use the numerical schemes developed in this paper to simulate the experimental results.

2 Field equations, boundary conditions and constitutive law for the impact problem of SMA rods

We consider a thin cylindrical rod of constant cross-section and length L. We associate with it a coordinate system with the origin being placed at the left end of the rod and the Ox axis directed along the rod. The material points of the rod occupy the interval $\Omega = \{x \in \mathbb{R} | 0 < x < L\}$, where x is the material or Lagrangian coordinate. The rod is initially stress free and is at rest. It is then subjected to an impact load at its left end ($x = 0$). The right end ($x = L$) remains stress free. The field equations and boundary conditions are presented next.

2.1 Field equations

The rod is assumed to be long enough so the stress $\sigma(x,t)$ is uniaxial and along with all other field variables depend only axial position and time. The axial component of the displacement i denoted by $u(x,t)$. We further assume linearized strain so the axial component of the strain $\varepsilon(x,t)$ is related to the displacement by $\varepsilon(x,t) = u_x(x,t)$. Finally, the density of the material ρ is assumed constant. The balance of linear momentum and energy then read (Graff, 1975; Malvern, 1977):

$$\rho u_{tt} = \sigma_x \tag{1}$$

$$\rho(\mathcal{U} + \frac{1}{2}(u_t)^2)_t = (u_t\sigma - q)_x \tag{2}$$

where $T(x,t)$ is the temperature, $\mathcal{U}(x,t)$ the internal energy per unit volume and $q(x,t)$ is the heat flux in the positive x direction. We shall consider two different types of boundary value problems depending on the difference in the transformation behavior of the SMA materials.

The timescale of the impact problem is on the order of micro- to milliseconds. Such time-intervals are too short for heat conduction to take place as well as for convection to remove heat trough the lateral surface of the rod. The physically meaningful initial-boundary value problems are either isothermal or adiabatic. The first is used if no significant heat is generated during the impact while the adiabatic problem is used otherwise.

The *isothermal* initial-boundary value problem is obtained from the field equations when we set constant temperature $T(x,t) = T_0$ throughout the rod. The balance of energy is identically satisfied and only the equation of motion (1) is considered. The initial conditions indicate that the rod is at rest:

$$u|_{t=0} = 0,\ u_t|_{t=0} = 0,\ \sigma|_{t=0} = 0 \tag{3}$$

The boundary conditions

$$\sigma|_{x=0} = \sigma_0(t),\ \sigma|_{x=L} = 0 \tag{4}$$

specify the impact stress $\sigma_0(t)$ [2] applied to the left end of the rod. The right end is kept stress free. Together (1), (3) and (4) form a well-posed hyperbolic problem (Bekker, 2001).

For the *adiabatic* approximation one assumes that no heat conduction occurs in the rod and no heat convection through the lateral surface. The heat conduction term q in (2) is equal to zero so the balance of energy in conjunction with (1) yield

$$\rho\mathcal{U}_t = \sigma u_{xt} \tag{5}$$

[2] We do not require continuity on $\sigma_0(t)$

The initial conditions for displacement and stress (4) are complemented by one more initial condition for the temperature:

$$T(x,0) = T_0 \tag{6}$$

where T_0 is the initial temperature assumed constant along the length of the bar. Thus the field equations (1),(5), initial conditions (4),(6) and boundary condition (3) define the adiabatic problem.

2.2 Constitutive law

In order to complete the field equations and be able to solve the boundary value problems we need to introduce a thermomechanical constitutive law that will connect the stress and internal energy with the evolution of strains and temperature. The hysteresis of the material is strongly dependent on the stress-temperature path that is followed during the loading cycle. In reality there are two distinct types(?) of martensite - twinned (self-accommodated) martensite M^t and detwinned M^d. The phase diagram for NiTi based SMAs is shown on Figure 1. The phase diagram and the possible phase transformations are explained in great detail in (Lagoudas and Shu, 1999). Let us briefly describe all three possible ways inelastic deformations occur:

- Austenite to twinned martensite ($A \to M^t$) and vice versa ($M^t \to A$). The phase transition occurs during cooling or heating the material. The crystal lattice changes from cubic in the austenite phase to monoclinic in the M^t phase. The four temperatures M^{of}, M^{os}, A^{os}, A^{of} that are shown on the phase diagram define the beginning and ending (at zero stress level) of this type of transformation.
- Austenite to detwinned martensite ($A \to M^d$) and vice versa ($M^d \to A$). The phase transition is triggered by increase or decrease of stress levels. The material behavior is referred to as pseudoelastic response if the loading path is a closed loop that starts and ends at the same point in the austenite region. These thermomechanical paths are also associated with large latent heat generation during the phase transitions. The stress induced forward transformation $A \to M^d$ is exothermic while the backward transformation $M^d \to A$ is endothermic (Cory, 1985; McNichols, 1987). A very simple subcase are the isothermal a) and adiabatic b) paths shown on Figure 1.
- Self-accommodated martensite to detwinned martensite ($M^t \to M^d$). This last type of inelastic deformation is not associated with a phase change but with stress induced reorientation of martensitic variants. It is irreversible upon unloading but the inelastic strains can be recovered if the material is heated above A^{of}. This is the basis of the Shape Memory Effect (SME) which

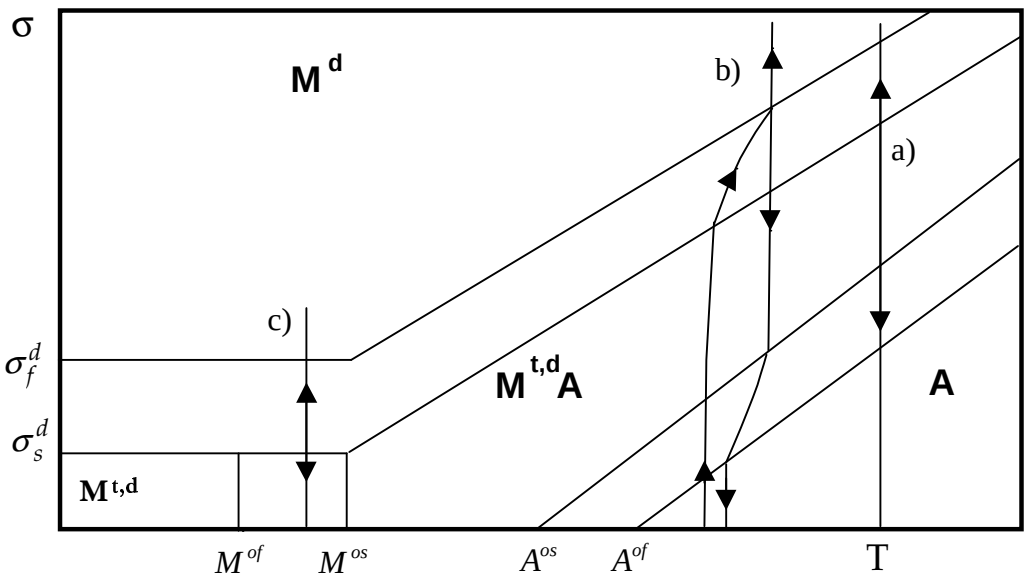

Fig. 1. Uniaxial stress phase diagram for a NiTi SMA material

we will not describe in details since it is outside the scope of our study. The material constants defining this transition are the initiating stress level σ_s and ending stress level σ^f. This deformation can occur only at temperatures below the M^{os}. It is not associated with any significant heat generation but the linear thermoelastic response

In this paper we use the theory introduced by (Lagoudas et al., 1996) which is formulated in terms of the Gibbs free energy G and employs the volume fraction of martensite ξ as an internal variable. The martensitic volume fraction ξ does not distinguish between the two types and denotes the volume fraction of M^d and M^t combined. Later we shall see how this reflects on the ability of the model to predict various thermomechanical paths. The general form of the free energy is taken to be:

$$\begin{aligned} G = G(\sigma, T, \xi) = & -\tfrac{1}{2\rho}\mathcal{S}\sigma^2 - \tfrac{1}{\rho}\left(\alpha(T - T_0) + \varepsilon^t\right) \\ & + c\left((T - T_0) - T\ln\left(\tfrac{T}{T_0}\right)\right) - s_0 T + u_0 + f(\xi) \end{aligned} \tag{7}$$

where ε^t inelastic transformation strain associated with the phase transformation. The function $f(\xi)$ is taken to be a quadratic polynomial and is responsible for the transformation hardening:

$$f(\xi) = \begin{cases} \frac{1}{2}\rho b^M \xi^2 + (\mu_1 + \mu_2)\xi, & \dot{\xi} > 0 \\ \frac{1}{2}\rho b^A \xi^2 + (\mu_1 - \mu_2)\xi, & \dot{\xi} < 0 \end{cases} \tag{8}$$

The material constants ρb^A, ρb^M, μ_1 and μ_2 define the transformation surfaces and the hardening during the forward and reverse transitions. The remaining material properties in (7) are effective compliance $\mathcal{S}$, effective thermal expansion coefficient α, effective specific heat c, effective specific entropy at the reference state s_0 and effective specific internal energy at the reference state u_0. They are chosen by the rule of mixtures (quantities with subscript A denote the appropriate material constant for the austenite phase and those with subscript M for the martensite phase):

$$\begin{aligned} \mathcal{S} = \mathcal{S}(\xi) &= \mathcal{S}^A + \xi(\mathcal{S}^M - \mathcal{S}^A) \\ \alpha = \alpha(\xi) &= \alpha^A + \xi(\alpha^M - \alpha^A) \\ c = c(\xi) &= c^A + \xi(c^M - c^A) \\ s_0 = s_0(\xi) &= s_0^A + \xi(s_0^M - s_0^A) \\ u_0 = u_0(\xi) &= u_0^A + \xi(u_0^M - u_0^A) \end{aligned} \tag{9}$$

The transformation strain ε^t with is connected with ξ through the relation

$$\varepsilon^t = H sgn(\sigma)\xi \tag{10}$$

where H is a positive material constant corresponding to the maximum transformation strain. Taking into account that $\varepsilon = -\frac{\partial G}{\partial \sigma}$ the following constitutive relation is obtained:

$$\sigma = E(\xi)(\varepsilon - \alpha(\xi)(T - T_0) - \varepsilon^t(\xi)) \tag{11}$$

where $E(\xi) = 1/\mathcal{S}(\xi)$.

The transformation condition is based upon thermomechanical transformation surfaces (see (Lagoudas et al., 1996)) which, in the 1-D case become the lines on the $\sigma - T$ diagram [3]. The principle of maximum transformation dissipation in conjunction with the second law of thermodynamics leads to the following transformation surface:

$$\begin{aligned} \sigma H + \tfrac{1}{2}\Delta\mathcal{S}\sigma^2 + \Delta\alpha\sigma(T - T_0) + \rho\Delta c\left((T - T_0) - T\ln\left(\tfrac{T}{T_0}\right)\right) \\ +\rho\Delta s_0 T - \tfrac{\partial f}{\partial \xi} - \rho\Delta u_0 = \pm Y^* \end{aligned} \tag{12}$$

[3] Note that they are not straight lines due to the presence of quadratic terms in (12).

where $Y^* = -\frac{1}{2}\rho\Delta\mathcal{S}(A^{of} - M^{os}) - \frac{1}{4}\rho\Delta\mathcal{S}(M^{os} - M^{of} - A^{of} + A^{os})$ and the $+Y^*$ at the right hand side stands for the forward transformation surface ($A \to M$) and $-Y^*$ for the reverse transformation surface ($M \to A$). This transformation surfaces accurately model the material response away from the detwinning range. When the thermomechanical loading path lies in the lower left part of the phase diagram the transformation surface (12) deviates from the actual one. (??? WE HAVE TO SAY SOMETHING ???)

The problem of latent heat generation becomes relevant if we consider that the timescale of the problems under consideration is on the order of micro- to milliseconds. Such time-intervals are too short for heat conduction to take place as well as for heat convection to remove the heat trough the lateral surface of the rod. Therefore dynamic loading with initial temperature $T > A^{of}$ and with stress levels high enough to cause phase transformation will involve latent heat release that cannot be dissipated in the surrounding environment. Therefore material points where sufficient latent heat is generated will change their position on the phase diagram and the material response at such points will subsequently be altered. The most appropriate setting for the impact problem in the pseudoelastic cases is the adiabatic initial-boundary value problem. On the other hand when the material is initially in M^t state the only possible inelastic deformation is detwinning of martensite so the isothermal initial-boundary value problem is sufficient for accurate physical description of the impact problem.

2.3 Detwinning of martensite

As mentioned earlier the model used in this paper does not distinguish between M^d and M^t. Consequently, the model can handle $A \leftrightarrow M^d$ and $A \leftrightarrow M^t$ and separately from them the detwinning transformation $M^t \to M^d$. Suppose that the material is completely in the M^t phase. During loading there will be no latent heat effects and the loading is effectively isothermal. Since there is no difference in the material constants between M^t and M^d the transformation criterion reduces to standard J_2 plasticity:

$$\sigma H - \frac{\partial f}{\partial \xi} = 0 \tag{13}$$

The martensitic volume fraction ξ now plays the role of the amount of detwinning strains and H is the maximum detwinning strain. The material constants in 7 trough 11 are taken to be the ones for martensite and only the forward portion of the transformation hardening function is used:

$$f(\xi) = \frac{1}{2}\rho b^d \xi^2 + Y^d \xi \tag{14}$$

The material constant b^d defines the hardening during the detwinning and $Y^d = \sigma_s H$ states that the onset of the deformation occurs at the critical stress level σ_s. The deformation is completed when $\xi = 1$ which implies that $\rho b^d = \sigma_f H - Y^d$. Any further loading causes only elastic response. This recalibration of the model allows us to use it effectively for detwinning transformations when no stress induced martensite is produced.

2.4 Isentropic approximation

With the constitutive model fully defined we will substitute the actual expression for the internal energy in (5) in order to further simplify the adiabatic heat equation. Let us express it in terms of the entropy S. We have

$$S = -\frac{\partial G}{\partial T},\ \varepsilon = -\rho\frac{\partial G}{\partial \sigma},\ \pi = -\rho\frac{\partial G}{\partial \xi} \tag{15}$$

where π is the driving force for the transformation. Now, using a Legendre transform $\mathcal{U} = G + TS + \rho^{-1}\sigma\varepsilon$ we rewrite (5) as

$$\rho T S_t = \pi \xi_t \tag{16}$$

Further, combining (7) and (15)the particular form of the entropy for SMA materials given in (Lagoudas et al., 1996) is

$$S = \alpha\sigma/\rho + C\ln(T/T_0) - \Delta s_0 \xi + s_0^A \tag{17}$$

where C is the heat capacity (equal for austenite and martensite) and for notational simplicity we introduced $\Delta s_0 = s_0^A - s_0^M$ to be the difference of the specific entropies for the two phases. On substituting (17) into (16) we find:

$$\rho C T_t = -T\left(\alpha\sigma - \rho\Delta s_0 \xi\right)_t + \pi\xi_t \tag{18}$$

According to (Cory, 1985; McNichols, 1987) $\pi \ll \rho\Delta s_0 T$ for most SMAs (e.g. for NiTi the precise values yield $\pi/\rho\Delta s_0 T \ll 1.3\%$) so we can approximate 18 by

$$\rho C T_t = -T\left(\alpha\sigma - \rho\Delta s_0 \xi\right)_t \tag{19}$$

which is equivalent to the isentropic condition $S_t = 0$. Equation 19 has the advantage that it can be integrated directly:

$$T = T_0 e^{-\frac{1}{\rho C}(\alpha(\xi)\sigma - \rho\Delta s_0 \xi)} \tag{20}$$

Here we explicitly stated the dependence of the temperature on the strain and stress.

2.5 Tangent moduli

In order to develop the displacement based FEM model in the next section we need to compute the increment of the stress with respect to an increment in the strain.

In the isothermal case the thermal contribution $\alpha(T - T_0)$ in (11) is zero hence (20) is identically satisfied so we have

$$\frac{d\sigma}{d\varepsilon} = \frac{\partial\sigma}{\partial\varepsilon} \tag{21}$$

In the adiabatic case however we have

$$\frac{d\sigma}{d\varepsilon} = \frac{\partial\sigma}{\partial\varepsilon} + \frac{\partial\sigma}{\partial T}\frac{dT}{d\varepsilon} \tag{22}$$

and in order to find the total derivative $\frac{d\sigma}{d\varepsilon}$ we need to express $\frac{\partial T}{\partial\varepsilon}$ in closed form. We do this by differentiating equations (11) and (20) with respect to the strain and combine the result to obtain:

$$\frac{dT}{d\varepsilon} = -\left(\alpha\frac{\partial\sigma}{\partial\varepsilon} + (\sigma\Delta\alpha - \rho\Delta s_0)\frac{\partial\xi}{\partial\varepsilon}\right) \Big/ \left(\frac{\rho C}{T} + \alpha\frac{\partial\sigma}{\partial T} + (\sigma\Delta\alpha - \rho\Delta s_0)\frac{\partial\xi}{\partial T}\right) \tag{23}$$

For compactness we introduced the notation $\Delta\alpha = \alpha^M - \alpha^A$. Second order approximations for the partial derivatives $\frac{\partial\sigma}{\partial\varepsilon}$, $\frac{\partial\sigma}{\partial T}$, $\frac{\partial\xi}{\partial\varepsilon}$ and $\frac{\partial\xi}{\partial T}$ are developed in (Qidwai and Lagoudas, 2000) and thus we are able to compute numerically the tangent moduli (21) and (22).

3 Numerical implementation

We begin with the numerical techniques used to implement the constitutive laws. For given strain increment $\Delta\varepsilon$ and temperature increment ΔT the stress σ given by equation (11) is computed with the help of the cutting plane return-mapping algorithm described in (Qidwai and Lagoudas, 2000). A displacement based FEM provides strain increments. For isothermal problems $\Delta T = 0$ and thus the cutting-plane algorithm computes the required value for the stress. In the adiabatic approximation however both the stress and temperature become dependent on the strain increment $\Delta\varepsilon$ that is, we have to simultaneously satisfy (11) and (20). This is done via an iterative process. We are given values $\varepsilon^{(0)}$, $\sigma^{(0)}$, $T^{(0)}$ for strain, stress and temperature which satisfy (11) and (20) and a strain increment $\Delta\varepsilon$. We then find (σ, T) corresponding to strain $\varepsilon = \varepsilon^{(0)} + \Delta\varepsilon$ trough the iteration $(\sigma^{(n)}, T^{(n)}) \to (\sigma, T)$ defined by:

$$\sigma^{(n+1)} = E\left(\varepsilon - \alpha\left(T^{(n)} - T_0\right) - \varepsilon^{t(n)}\right) \tag{24}$$

$$T^{(n+1)} = T_0 e^{-\frac{1}{\rho C}\left(\alpha\sigma^{(n+1)} - \rho\Delta s_0 \xi^{(n+1)}\right)} \tag{25}$$

The first equation (24) uses the return-mapping algorithm to compute a new value $\sigma^{(n+1)}$ for the stress based on the old temperature $T^{(n)}$. The second equation (25) attempts to enforce the isentropic heat equation by computing a corrected temperature $T^{(n+1)}$. The process is terminated when there is no further progress, i.e. when $\left|\sigma^{(n+1)} - \sigma^{(n)}\right|$ and $\left|T^{(n+1)} - T^{(n)}\right|$ both drop below certain tolerance. The algorithm showed linear convergence in the test cases, however a detailed theoretical study is required to establish its properties.

3.1 FEM procedure

A standard semi-discrete Galerkin approximation is used to generate the weak form of the problem:

Find $u^h(x,t) = \sum_{i=1}^{N} U_i(t)\psi_i(x)$ such that:

$$\rho\int_0^L \ddot{u}^h v^h dx + \int_0^L \sigma v^h_{,x} dx = -\sigma v^h\Big|_{x=0} \tag{26}$$

Throughout this paper we used linear elements, that is:

$$span(\psi_1, ..., \psi_N) = P^1([0, L]) \subset H^1([0, L])$$

As usual we have $N-1$ number of elements (i.e. N nodes), the nodal values for the displacement are given by $U_i(t)$ and whenever appropriate, we shall use vector notation, i.e. $\mathbf{U} = (U_1, ..., U_N)^t$.

The problem reduces to a second order nonlinear system of ODEs:

$$\mathbf{M}\ddot{\mathbf{U}} + \mathbf{K}_{\xi(t)}(\mathbf{U})\mathbf{U} = \tilde{\mathbf{F}}_{\xi(t)}(\mathbf{U}) \tag{27}$$

where $\mathbf{M}$ is the mass matrix, $\mathbf{K}_{\xi(t)}(\mathbf{U})$ the stiffness matrix and $\tilde{\mathbf{F}}_{\xi(t)}(\mathbf{U})$ is the forcing term due to the nonlinear and thermal strains. The subscript $\xi(t)$ stands to indicate that $\tilde{\mathbf{F}}_{\xi(t)}(\mathbf{U})$ and $\mathbf{K}_{\xi(t)}(\mathbf{U})$ do not depend on the displacement only but on the whole loading history. However, for any given loading history the stress and hence $\mathbf{K}(\mathbf{U})$ and $\tilde{\mathbf{F}}(\mathbf{U})$ can be viewed as well defined single valued functions. Thus, without loss of generality we shall drop the subscript $\xi(t)$ in the discussion that follows. They are given by:

$$M_{ij} = \rho \int_0^L \psi_i \psi_j dx \tag{28}$$

$$K_{ij}(\mathbf{U}) = \int_0^L E(\xi) \frac{\partial \psi_i}{\partial x} \frac{\partial \psi_j}{\partial x} dx \tag{29}$$

$$\tilde{F}_i(\mathbf{U}) = \int_0^L E(\xi) \left[\varepsilon^t(\xi) + \alpha(\xi)(T - T_0)\right] \frac{\partial \psi_i}{\partial x} dx \tag{30}$$

We introduce $\mathbf{F}(\mathbf{U}) = \tilde{\mathbf{F}}(\mathbf{U}) - \mathbf{K}(\mathbf{U})\mathbf{U}$ which is the full forcing term [4]:

$$\mathbf{F}_i(\mathbf{U}) = -\int_0^L \sigma \frac{\partial \psi_i}{\partial x} dx \tag{31}$$

Equation (27) can be rewritten as

$$\mathbf{M}\ddot{\mathbf{U}} = \mathbf{F}(\mathbf{U}) \tag{32}$$

The time integration in (32) (or (27))is done by the backward difference method, a member of the Newmark family (Newmark, 1959; Reddy, 1993). For $t = t_s$ the Newmark scheme is defined by [5]:

$$\mathbf{U}_{s+1} = \mathbf{U}_s + \tau \dot{\mathbf{U}}_s + \frac{1}{2}\tau^2((1-\gamma)\ddot{\mathbf{U}}_s + \gamma \ddot{\mathbf{U}}_{s+1}) \tag{33}$$

$$\dot{\mathbf{U}}_{s+1} = \dot{\mathbf{U}}_s + \tau((1-\alpha)\ddot{\mathbf{U}}_s + \alpha \ddot{\mathbf{U}}_{s+1}) \tag{34}$$

[4] Similarly, a more precise notation for $\mathbf{F}(\mathbf{U})$ would be $\mathbf{F}_{\xi(t)}(\mathbf{U})$

[5] The usual notation $\mathbf{U}_s := \mathbf{U}(t_s)$ is used

The backward difference method is obtained by setting $\alpha = \frac{3}{2}$ and $\gamma = 2$. It is easy to show (see (Reddy, 1993)) that the above difference equations lead to the following system of nonlinear algebraic equations for U_{s+1}:

$$\frac{2}{\gamma\tau^2}\mathbf{M}\mathbf{U}_{s+1} = \mathbf{F}(\mathbf{U}_{s+1}) + \mathbf{G}_s \tag{35}$$

or, equivalently to

$$\left(\frac{2}{\gamma\tau^2}\mathbf{M} + \mathbf{K}(\mathbf{U}_{s+1})\right)\mathbf{U}_{s+1} = \tilde{\mathbf{F}}(\mathbf{U}_{s+1}) + \mathbf{G}_s \tag{36}$$

where $\mathbf{G}_s = \mathbf{M}\left(\frac{2}{\gamma\tau^2}\mathbf{U}_s + \frac{2}{\gamma\tau}\dot{\mathbf{U}}_s + \frac{1-\gamma}{\gamma}\ddot{\mathbf{U}}_s\right)$. The nonlinear problem (35) is solved by a quasi-Newtonian algorithm. The right-hand side is linearized:

$$F_i(\mathbf{U} + \Delta\mathbf{U}) \simeq F_i(\mathbf{U}) + \sum_{j=1}^{N}\frac{\partial F_i(\mathbf{U})}{\partial U_j}\Delta U_j$$

and further the chain rule is used to obtain:

$$L_{ij}(\mathbf{U}) := \frac{\partial F_i(\mathbf{U})}{\partial U_j} = \int_0^L \frac{\partial\sigma}{\partial U_j}\frac{\partial\psi_i}{\partial x}dx = \int_0^L \frac{d\sigma}{d\varepsilon}\frac{\partial\psi_j}{\partial x}\frac{\partial\psi_i}{\partial x}dx \tag{37}$$

Numerically $\mathbf{L}$ is evaluated by substituting the appropriate expression for $\frac{d\sigma}{d\varepsilon}$, that is we use (21) in the isothermal case and (22) in the adiabatic case.

The solution $\mathbf{U}_{s+1}$ is found through a Newton-Raphson iterative process. We set $\mathbf{U}_{s+1}^{(0)} = \mathbf{U}_s$ and for $n = 1, 2\ldots$ until convergence we compute:

$$\mathbf{U}_{s+1}^{(n+1)} = \left(\frac{2}{\gamma\tau^2}\mathbf{M} - \mathbf{L}(\mathbf{U}_{s+1}^{(n)})\right)^{-1}\left(\mathbf{F}(\mathbf{U}_{s+1}^{(n)}) - \mathbf{L}(\mathbf{U}_{s+1}^{(n)})\mathbf{U}_{s+1}^{(n)} + \mathbf{G}_s\right) \tag{38}$$

Of the two algorithms presented in (Qidwai and Lagoudas, 2000) we chose the cutting plane method. For this method the partial derivatives are derived in approximate form. Thus we get a quasi-Newton algorithm which showed local quadratic convergence for small enough time-steps. In the case when convergence was being lost we applied the Picard (simple) iteration to (36). Again, set $\mathbf{U}_{s+1}^{(0)} = \mathbf{U}_s$ and for $n = 1, 2\ldots$ until convergence compute:

$$\mathbf{U}_{s+1}^{(n+1)} = \left(\frac{2}{\gamma \tau^2} \mathbf{M} + \mathbf{K}(\mathbf{U}_{s+1}^{(n)}) \mathbf{U}_{s+1}^{(n)} \right)^{-1} \left(\tilde{\mathbf{F}}(\mathbf{U}_{s+1}^{(n)}) + \mathbf{G}_s \right) \tag{39}$$

In all numerical examples tested the later iteration demonstrated global linear convergence.

3.2 Adaptive mesh refinement

Let σ_n^h be the stress at the end of the Newton algorithm at time step n, i.e. $t = t_n$. For linear elements σ^h is a piecewise constant function. Let us take $\overline{\sigma}^h$ to be the continuous, piecewise linear function in $[0, L]$ which assumes the averaged value of σ^h at each nodal point. It has been shown in (Zienkiewicz, 1987) that for linear problems one has the convergence result:

$$\left\| \overline{\sigma}^h - \sigma^h \right\|_{0,[0,L]} \to 0 \text{ as } \left\| U - U^h \right\|_{0,[0,L]} \to 0 \tag{40}$$

The above norms can be localized over each element through the obvious relation $\left\| \overline{\sigma}^h - \sigma^h \right\|_{0,[0,L]}^2 = \sum_e \left\| \overline{\sigma}^h - \sigma^h \right\|_{0,e}^2$. The estimator is then defined on the element level. For each element e we require that

$$\frac{\left\| \overline{\sigma}^h - \sigma^h \right\|_{0,e}}{\left\| \sigma^h \right\|_{0,[0,L]}} < TOL \tag{41}$$

We would like to emphasize two aspects of the actual implementation details of the FE analysis. The linear system (35) (or (36)) is tridiagonal and poses no computational problems. Secondly, the two most time-consuming parts of the FE procedure are the assembly of the stiffness matrix at each Newton step (because of the nonlinear dependance of the stiffness on the strain) and the force vector. Both of them require the execution of the stress update procedure via the return-mapping algorithm which is a computationally expensive operation and is preformed for each element at each Newton step.

Clearly a global uniform h-refinement strategy used to achieve satisfactory spatial discretization will impose severe restrictions on the problem size due to the assembly time issues. In order to avoid this we used the Zienkiewicz-Zhu error estimator to perform adaptive meshing. The local criterion (41) is applied to each element at the completion of the Newton iteration. If there is no further need to refine the mesh we proceed to the next time step. We found that this approach works very well for the class of SMA hysteretic materials under consideration.

Table 1
Material parameters used in the SMA model

Material constant	Value	Description
E^A	70×10^9 Pa	Modulus of elasticity in austenite
E^M	30×10^9 Pa	Modulus of elasticity in martensite
H	0.05	Maximum transformation strain
$\frac{d\sigma}{dT}$	$7.0 \times 10^6\ Pa/(m^3K)$	
M^{of}	$2\ ^\circ C$	Martensitic finish temperature
M^{os}	$18\ ^\circ C$	Martensitic start temperature
A^{os}	$22\ ^\circ C$	Austenitic start temperature
A^{of}	$42\ ^\circ C$	Austenitic finish temperature

4 Numerical Examples

We tested the implementation of the FEM in two different model problems. The fixed impact stress model problem presented in the next section involves only the loading part of the hysteresis and is therefore representative for both isothermal and adiabatic thermomechanical paths (Figure 2). Further, the main difference in the shape of the hysteresis loop for stress-induced martensite and detwinning of martensite is the unloading part. Therefore, when we only have loading it is sufficient to test only isothermal thermomechanical paths.

The second model problem that is considered is one for a square pulse. In this case the shape of the unloading part of the hysteresis is important. In order to stay close to the physical reality we tested two thermomechanical parts: an adiabatic path in pseudo-elastic regime ($T > A^{of}$) and an isothermal at temperatures $T < M^{os}$. The first part is interesting with the fact that it provides full shape recovery. The later path gives important insight into the wave structure of the solution in the detwinning range. We shall later encounter this type of thermomechanical paths in the modelling of the Hopkinson bar experiment (Sections 5 and 6).

The material properties (Table 1) for all model problems are taken from (Qidwai and Lagoudas, 2000) and represent generic NiTi SMA properties. In addition to that for all model problems we had:

- 50cm NiTi SMA rod in an isothermal setup was considered
- Total simulation time was $100\mu s$ so that the elastic front would not reach the fixed right end of the rod
- All calculations were performed on a 933 Mhz PIII machine running Windows NT.

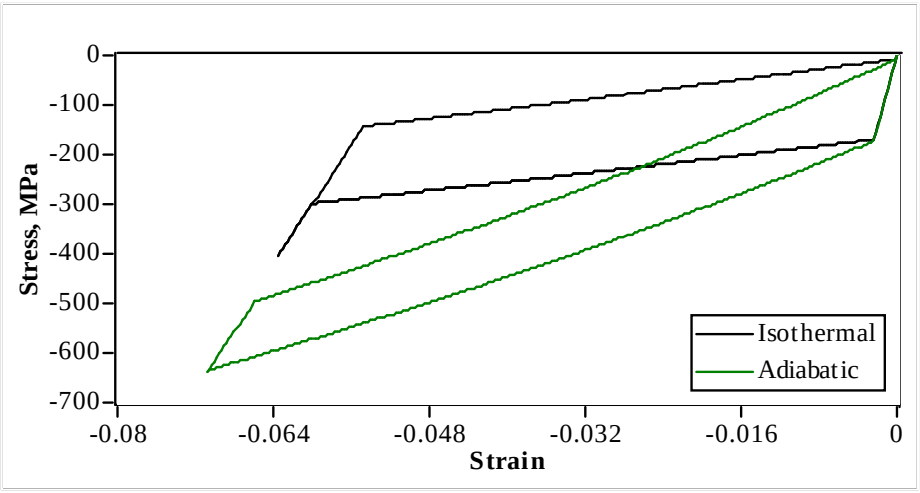

Fig. 2. An adiabatic and isothermal path for the material data in Table 1 at $T = 47\ ^{\circ}C$. Under adiabatic conditions higher stress levels are required to complete the phase transformation compared to isothermal hysteresis loops.

4.1 Fixed impact stress model problem

The fixed impact stress initial-boundary value problem [6] is defined by setting the boundary condition to be the two constant-state function:

$$\sigma_0(t) = \begin{cases} 0 & \text{for } t \leq 0 \\ \sigma_0 & \text{for } t > 0 \end{cases} \tag{42}$$

We chose this particular boundary condition because the it is a natural starting point for nonlinear hyperbolic equations and because there are existing analytical solutions for it. Following (Bekker et al., 2002; Chen and Lagoudas, 2000) one can show that the following two-shock solution:

$$g(x,t) = \begin{cases} g_{ph} & \text{for } \quad 0 \quad \leq x \leq V_{ph}t \\ g_{el} & \text{for } V_{ph}t < x \leq V_{el}t \\ 0 & \text{for } V_{el}t < x \leq L \end{cases} \tag{43}$$

where $g = v, \sigma, \varepsilon$ and $\sigma_{ph} = \sigma_0$.

[6] When the same initial boundary value problem is reformulated as an initial problem on an infinite domain with the initial condition being a step function it is usually referred to as the *Riemann* problem.

The pair $(\varepsilon_{el}, \sigma_{el})$ is the point on the hysteresis curve that corresponds to the start of the phase transformation.

The faster shock is a linear elastic shock and has velocity

$$V_{el} = \sqrt{\frac{\sigma_{el}}{\rho \varepsilon_{el}}} = \sqrt{\frac{E^A}{\rho}} \tag{44}$$

The second, slower shock, is the transformation shock which travels with velocity

$$V_{ph} = \sqrt{\frac{\sigma_0 - \sigma_{el}}{\rho(\varepsilon_0 - \varepsilon_{el})}} \tag{45}$$

This later shock specifies the point of abrupt phase transition - for $x \leq V_{ph}t$ the material is an martensite and in the region $x \geq V_{ph}t$ it it still in the austenite phase. This is a truly self contained nonlinear shock because of the convex-down nature of the function $\sigma(\varepsilon)$ for $\varepsilon > \varepsilon_{el}$. For a general discussion on the solution to the Riemann problem in nonlinear hyperbolic PDEs (Godlewsky and Raviart, 1996, pg. 83-97). For a discussion specific to SMA materials the reader is referred to (Chen and Lagoudas, 2000; Bekker, 2001).

For this model problem we set $\sigma_0 = 400MPa$ and $T = 47\ ^\circ C$. Given this and the material data one can compute the exact speed of the shocks:

$$V_{ph} = 723m/s \tag{46}$$
$$V_{el} = 3294m/s \tag{47}$$

The corresponding stress levels are $\sigma_{ph} = 400MPa$ and $\sigma_{el} = 195MPa$.

The first thing to be observed when using a fixed mesh was the expected two-shock structure of the solution. Results for two different mesh sizes are given in Figure 3. We tested several members of the Newmark family and found that best results are given by the backward difference method. Of the others, explicit methods as well as the constant acceleration scheme were unconditionally unstable. Of those that were able to converge the backward difference was found to dampen the hight frequency oscillations (Figure 3, left) in the most efficient manner while introducing reasonable amounts of numerical dissipations, mostly visible at the elastic shock. The quasi-Newton method used to solve the nonlinear system (35) showed quadratic convergence at all time steps but the first few ones. In that case we used the alternative direct iteration (39).

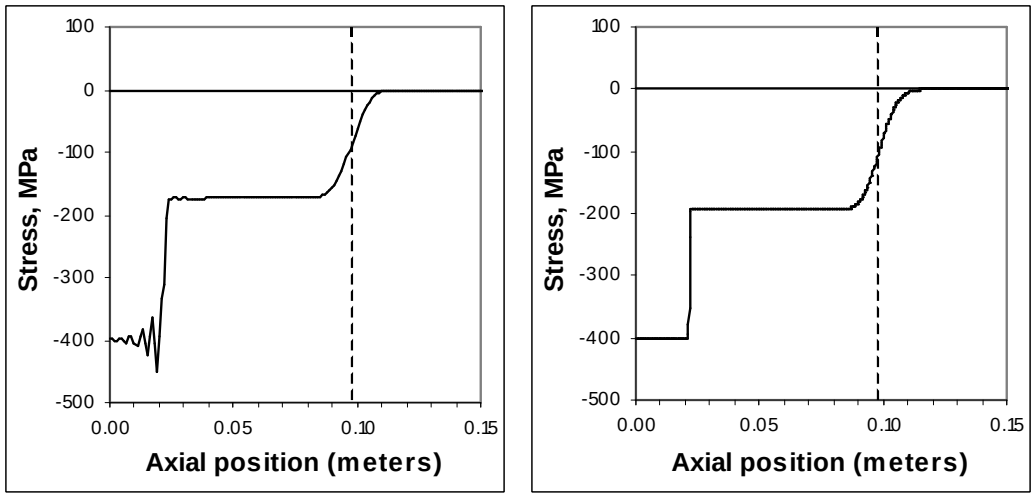

Fig. 3. Stress profile at $30\mu s$ for a fixed mesh with 500 (left) and 2000 elements (right). Wiggles are eliminated for the finer spatial discretization. The position of the elastic shock is marked by a dashed line.

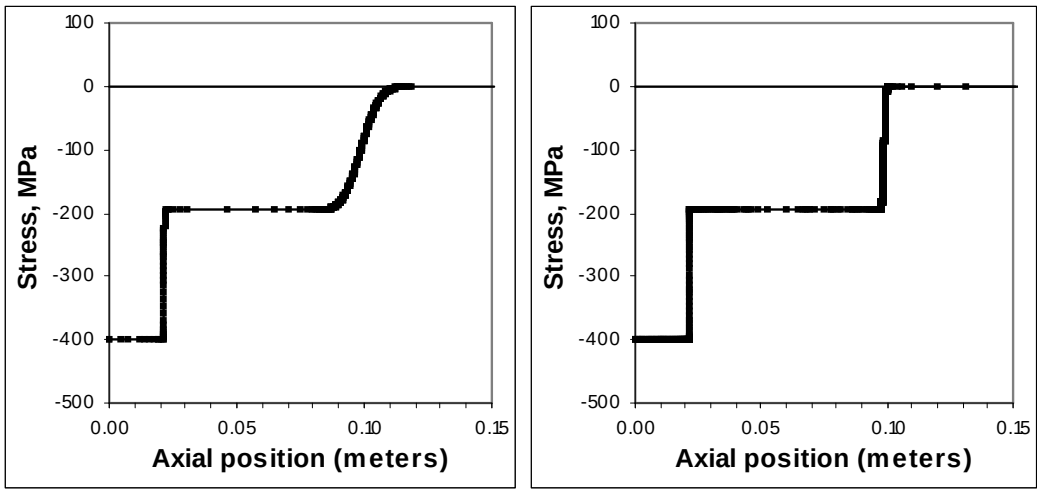

Fig. 4. Stress profile at $30\mu s$ for an adaptive mesh with two different time steps. The linear shock is quite smeared for a coarse time step $\tau = 0.1\mu s$ (left) while it is much sharper when a finer step of $\tau = 0.001\mu s$ is used. Mesh nodes are marked with black squares.

Quantitativly the results obtained by the FEM are in agreement with the analytical solution. For a given time step both adaptive meshes and sufficiently fine fixed meshes deliver the same solution. For a time step of $\tau = 0.1\mu s$ the numerical value for the phase shock is found to travel with velocity in the range $693 - 900m/s$. The velocity of the elastic front is calculated to be in the range $3316 \pm 420m/s$. The smearing of the stress profile in the region of the elastic shock is due to the time-integration scheme. When the time step is decreased the slope becomes steeper and eventually converges to the shock. For an adaptive solution with a time step $\tau = 0.001\mu s$ (the same computation for a fixed mesh and such a time step was time prohibitive, see next paragraph)

Table 2
Execution times for fixed and adaptive meshes

Time	**Fixed Mesh**		**Adaptive Mesh**	
	Elements	Time (min)	Elements	Time (min)
10 μs	16000	56	161	1:12
20 μs	16000	113	199	2:37
40 μs	16000	226	256	6:10
80 μs	16000	451	301	15

the calculated values for the phase shock are now in the range $723 - 733 m/s$ and the elastic shock is within the bounds $3256 - 3366 m/s$. This indicates that the lower bound for the transformation shock is very close to the actual value (46) and the the elastic shock (47) is virtually in the middle of the suggested numerical range. Secondly the error in the predicted value for the phase shock decreases from 24% for $\tau = 0.1\mu s$ down to 1.3% for $\tau = 0.001\mu s$. The error in the elastic shock decreases from 12% to 1.1% which is a clear indication that the algorithm is converging. Of course a theoretical analysis is required to prove that.

A comparison for the two different meshes on Figure 3, both for a fixed time-step of $\tau = 0.1\mu s$ at time $t = 30\mu s$ shows that wiggles can be eliminated by refining the mesh. One can also see that there are big regions in the bar with no variation in the stress. This is fully utilized by the adaptive approach. Figure 4 shows an adaptive FE solution with the same time parameters as above and tolerance (see equation (41)) set to 10^{-4} such that the accuracy is comparable to the one of the fixed mesh with 2000 elements.

A more drastic comparison in the performance of the fixed and adaptive FE methods is given in Table 2. The time step is $\tau = 0.01\mu s$ and the number of elements for the fixed FEM is chosen so that the two solutions have comparable accuracy. Both numerical solutions in this case are much more accurate than the previous example because the smaller time step reduces the dissipation in the elastic shock. A comparison of the execution times for the fixed and adaptive methods shows that the adaptive procedure delivers an order of magnitude improvement in performance.

4.2 Energy dissipation for a square pulse

A more realistic initial-boundary value problem is one for which we do not have continuous constant loading but a square pulse, i.e.

$$\sigma_0(t) = \begin{cases} 0 \quad \text{for} \quad t \leq 0 \\ \sigma_0 \text{ for} \quad 0 < t < T_{pulse} \\ 0 \quad \text{for} \quad t \geq T_{pulse} \end{cases} \tag{48}$$

where T_{pulse} is the duration of the pulse. Unfortunately to the best of the authors knowledge, there are no known analytical solutions for this problem. Moreover, there are unresolved questions regarding the uniqueness of the weak solution for times $t > T_{pulse}$ when unloading takes place.

For this type of boundary condition which is much closer to practical cases we can evaluate the energy dissipation due to phase transformation. If we define $P(\tau)$ to be the work done by the external forces at left end of the rod from $t = 0$ to $t = \tau$, $\mathcal{K}(\tau)$ to be the kinetic energy of the rod (at time $t = \tau$) and $\mathcal{U}(\tau)$ be the strain energy of the rod then we have the obvious relations

$$\begin{aligned} P(\tau) &= \int_0^\tau \sigma(0,t)\dot{u}(0,t)dt \\ \mathcal{U}(\tau) &= \tfrac{1}{2}\int_0^L \sigma(x,\tau)\varepsilon(x,\tau)dx \\ \mathcal{K}(\tau) &= \tfrac{1}{2}\int_0^L \rho(\dot{u}(x,\tau))^2 dx \end{aligned} \tag{49}$$

and thus the energy dissipation can be defined as

$$D(\tau) = \frac{P(\tau) - (\mathcal{K}(\tau) + \mathcal{U}(\tau))}{P(\tau)} \tag{50}$$

In our numerical calculations we only used the adaptive FEM procedure as the examples in the previous subsection indicated that both the fixed and adaptive method give the same solution but at much different computational cost. In all numerical simulation we took $T_{pulse} = 10\mu s$. We explored to different loading conditions.

4.2.1 Adiabatic loading

The stress level used for the model problem was $\sigma_0 = 800MPa$ and the initial temperature was $T_0 = 47\ ^\circ C > A^{of}$. The stress level was chosen so that the full hysteresis loop could be realized (see Figure 2).

The most noticeable feature observed is the structure of the unloading pulse. Again we see a two wave shock structure that corresponds to the initial elastic

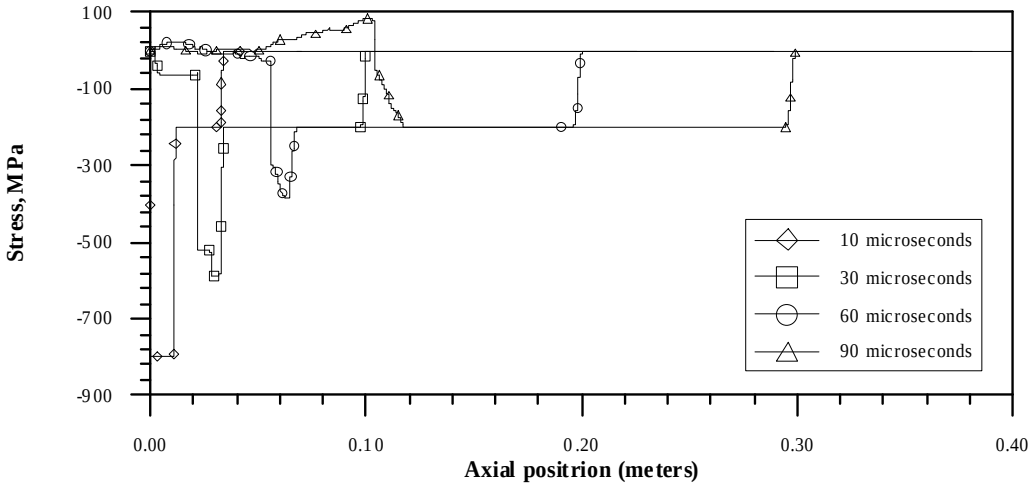

Fig. 5. Stress profile at different instances of time for a square pulse in adiabatic loading

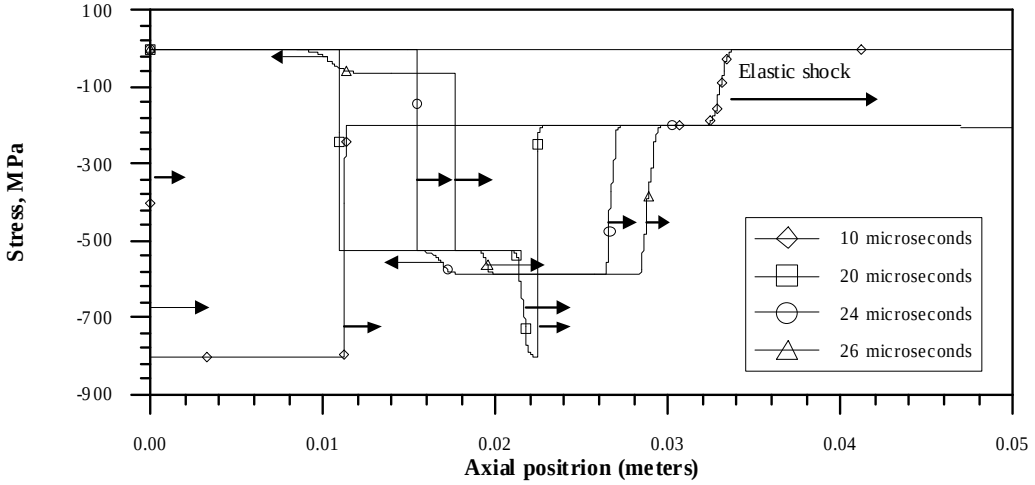

Fig. 6. Exploded view near the left end. The unloading ($10\mu s$) produces two right-travelling shock waves ($20\mu s$). The faster unloading wave reflects off the transformation shock ($\approx 21\mu s$) and forms a left-travelling wave ($24\mu s$). What follows is a series of complicated reflections that gradually kills the initial non-linear shock.

unloading and the following reverse transformation $M^t \rightarrow A$. both of them travel faster then the phase transformation shock. When the faster unloading front catches up with it a left-travelling reflection is generated. Left-travelling waves then partially reflect from the slower unloading shock and partially continue to bounce off the left end of the rod which is now stress free. A complicated series of reflections and/or rarefication waves follows. The first of them is shown in Figure 6. Due to lack of theoretical knowledge it is not possible to tell wether the reflected waves are shock pulses or rarefaction waves. The first reflection results in approximately 34% decrease of the peak stress level. The picture becomes even more complicated when the slower unloading shock eventually catches up with the forward travelling phase transformation shock. The evolution of the stress profile up to $90\mu s$ is shown on Figure 5.

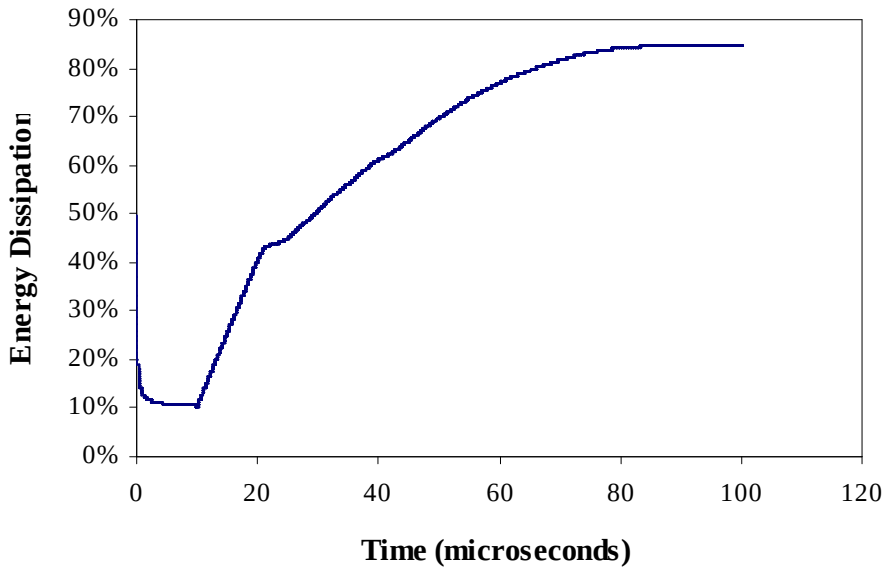

Fig. 7. Energy dissipation for a 10 μs square pulse in adiabatic conditions.

The calculation show that dissipation levels goes from 10% at the end of the pulse ($T = 10\mu s$) to 42% at $T \approx 22\mu s$ when the faster unloading wave hits the forward travelling transformation wave. The high stress levels are then gradually reduced within the elastic limits. The energy dissipation reaches approximately 80% at 100 μs, shortly before the elastic front reaches the right end.

4.2.2 Detwinning

The last model problem to be solved involved a simulation of the detwinning process in SMA materials. The polynomial model was not originally designed to take detwinning into account. However, if the material is in the austenite state and the temperature is in the range $M^{os} < T < A^{os}$ the resulting hysteresis due to phase transformation as predicted by the model will be close to the actual stress-strain relationship due to detwinning. A detailed discussion on how to use the polynomial model to to predict detwinning is given in Section 5.4. In this numerical simulation the initial temperature is set to $T_0 = 22\ ^\circ C$. The stress pulse has magnitude $\sigma_0 = 400MPa$ which is sufficient to complete the detwinning and then obtain the elastic response of the M^d phase. This implies that again we must expect a two forward propagating shocks as in the previous adiabatic case. The unloading is completely elastic and we expect to see a single linear shock, travelling fast enough to catch up with the nonlinear shock caused by the detwinning. This is followed by a series of reflections between the left end (which is stress free after the pulse is over) and the forward propagating detwinning shock. The stress profile at several different instances of time is presented on Figure 8 and completely matches

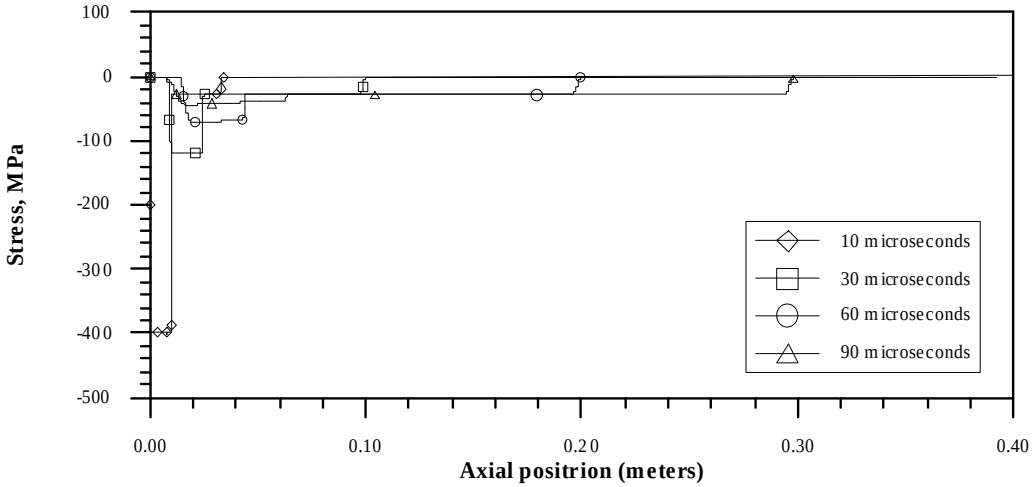

Fig. 8. Stress profiles at various times for a square pulse. The material is the detwinning range. The attenuation of the stress to values within the elastic material response is clearly visible.

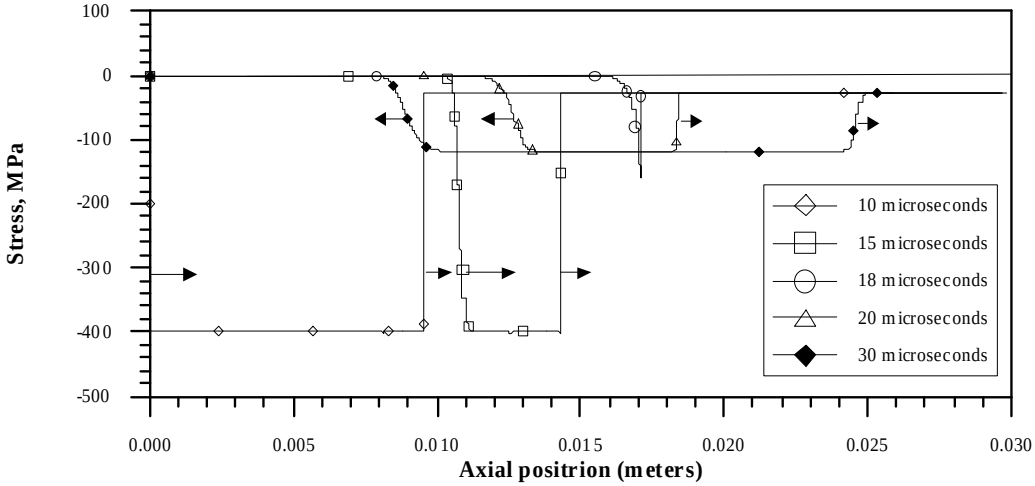

Fig. 9. Exploded view of stress profiles in the region close to the left end of the rod. Direction of the shock velocities are indicated by arrows.

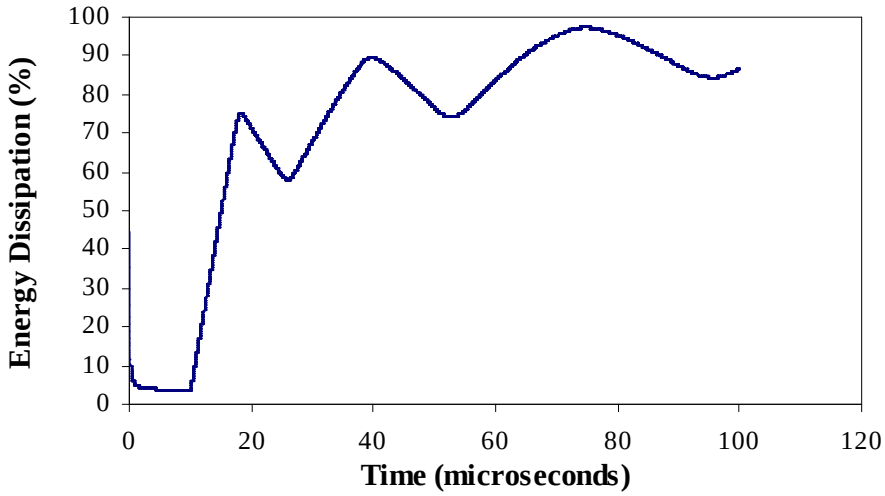

Fig. 10. Energy dissipation for a 10 μs square pulse.

the expectations.

Due to sequence of elastic waves reflecting off the left end (which cause the stress to reverse sign) and off the detwinning (nonlinear) shock the energy dissipation as a function of time (Figure 10) has a more complicated structure. The dissipation quickly reaches $\approx 75\%$ as the initial unloading wave reaches the nonlinear shock and reflects back (Figure 9). After each reflection off the left end the stress changes sign and in effect nullifies with the left travelling wave which causes a rise in the dissipation levels. Then the right-travelling reflections reach the nonlinear shock, cause it to decrease further and reflect as compressive left travelling waves causing a drop in the dissipation. It should be noted that even though in the long term the dissipation stabilizes around to 90% the material is permanently deformed. In order to recover its shape it has to be reheated.

5 Dynamic material characterization

The dynamic response of a nearly equiatomic NiTi alloy rod was characterized with one dimensional wave propagation experiments in a Hopkinson bar arrangement. We now turn to a description of this experiment.

5.1 Description of the Apparatus

Hopkinson bar apparatus has become standard in the characterization of the dynamic response of materials; detailed descriptions are provided in many handbooks and textbooks e.g. (Graff, 1975, pg. 128-134), and hence we provide only a brief description here. A photograph of the experimental setup is shown in Figure 11 and a schematic of the impact device is given in Figure 12.

The apparatus consists of a striker bar, an input bar and an output bar, all of diameter d = $15.5mm$ and all made of a 4340 steel, quenched and tempered to a martensitic state. The yield strength of these bars is about 1.8 GPa and they remain elastic during the impact experiments. The density of the bars is $\rho = 7800kg/m^3$, the measured bar wave speed $C_b = \sqrt{E_b/\rho} = 5300m/s$ and E_b is the modulus of elasticity of the steel bar. The striker bar (12) of length L is propelled from an air gun at speeds in the range of 10 to 40 m/s. This striker impacts the input bar which is $1.7m$ long; a one dimensional compression wave propagates into both bars; since the striker bar is short, the reflected tension pulse arrives at the striker-input bar interface at a time $T_{pulse} = 2L/C_b$; at this point, the striker comes to a stop and is disengaged from the input bar. Hence, a compression pulse of duration T_{pulse} is propagated down the length

Fig. 11. Photograph of the Hopkinson bar experimental setup. The specimen is visible at the top-right part of the photograph

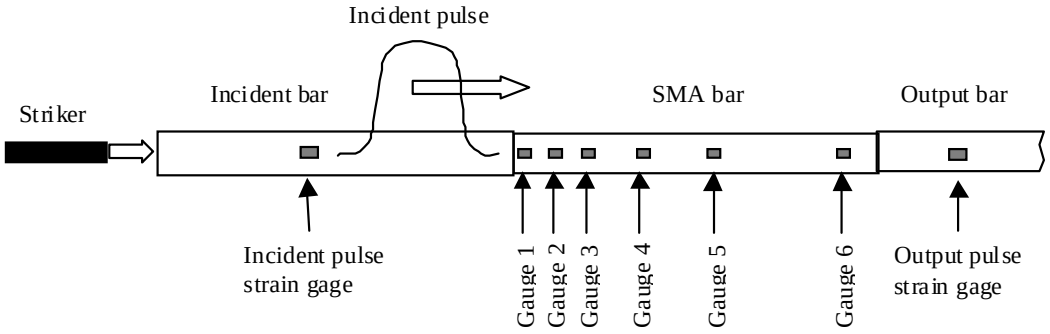

Fig. 12. Geometry and arrangement of strain gauges in Hopkinson apparatus. (Figure not drawn to scale)

of the input bar. This wave is coupled into the specimen which is in contact with the far end of the input bar. Due to the impedance mismatch between the specimen and the input bar, a part of the pulse is reflected back into the input bar and a part of the pulse propagates into the specimen. A strain gage mounted at about the middle of the input bar is used to monitor the incident compressive pulse and the reflected tensile pulse propagating in the input bar. The wave propagating through the specimen, gets coupled into the output bar, again with a reflected component due to the impedance mismatch. The output bar is free at the far end and so a tensile pulse reflects from the far end of the

output bar and is unable to transmit into the specimen; hence the specimen is loaded for only once. A strain gage mounted at the middle of the output bar is used to monitor the strain pulses, in particular the first transmitted pulse, in the output bar.

The main feature of the Hopkinson implementation of the dynamic experiment is in the length of the specimen, L_{sp} which is quite long. This means that a steady-state condition is not reached during the time T_{pulse} and one has to deal with the propagation of the wave in the specimen material.

5.2 Specimen Preparation

In our experiments we used a single SMA specimen 345 mm long and two short specimens of 25.4 mm length. All the specimens had diameter was 12.7 mm. After machining the specimens to the appropriate lengths they were heated to 540 $^{\circ}C$ in standard atmosphere for 2 hours and furnace cooled. This process was used to erase history of prior plastic deformation. A thin oxide layer was formed during the heat treatment, but this does not affect the overall response of the material. In the long bar, six strain gauges were placed at distances 10 mm, 20 mm, 40 mm, 80 mm, 160 mm and 320 mm from the impact end. A high temperature strain gauge adhesive was used and the specimens were then annealed at 100 C for 1 hour. Subsequently, the specimens were cooled to dry ice temperature (-70 $^{\circ}C$) and then brought to room temperature for testing. All tests were performed at room temperature (nominally 20 $^{\circ}C$) unless specified otherwise. A Differential Scanning Calorimeter (DSC) was used to determine the transformation temperatures in the material. As can be seen from the DSC measurements shown in Figure 13, under the indicated temperature cycling, the specimens were in a twinned martensitic state during the test. In order to obtain preliminary information on the mechanical behavior of this material quasi-static compression tests were performed on the short specimens in a standard testing machine. The first quasi-static test was performed at room temperature to obtain the critical stress values σ_s and σ_f for onset and finish of detwinning as well as the transformation hardening constants (Table 3). A second quasi-static test at elevated temperature ($T = 60\ ^{\circ}C$) was used to get the elastic modulus of the austenite phase.

The stress-strain relationship obtained from the quasi-static test at room temperature is shown in Figure 14 along with the predictions of the polynomial model; the initial elastic modulus can be estimated to be $42GPa$; beyond about 0.3% strain level, nonlinear response is observed and this corresponds to detwinning of the martensite. At about 3% strain, there is a sharp increase in the tangent modulus that corresponds to the exhaustion of detwinning.

Table 3
Material parameters used in the SMA model

Material constant	Value	Description
E^A	70×10^9 Pa	Modulus of elasticity in austenite
E^M	42×10^9 Pa	Modulus of elasticity in martensite
H	0.03	Maximum transformation strain
$\frac{d\sigma}{dT}$	$7.0 \times 10^6\ Pa/(m^3K)$	
M^{of}	6 $^\circ C$	Martensitic finish temperature
M^{os}	29 $^\circ C$	Martensitic start temperature
A^{os}	37 $^\circ C$	Austenitic start temperature
A^{of}	53 $^\circ C$	Austenitic finish temperature
σ_s	150MPa	Start of $M^t \leftarrow M^d$ transition
σ_f	280MPa	Completion of $M^t \leftarrow M^d$ transition

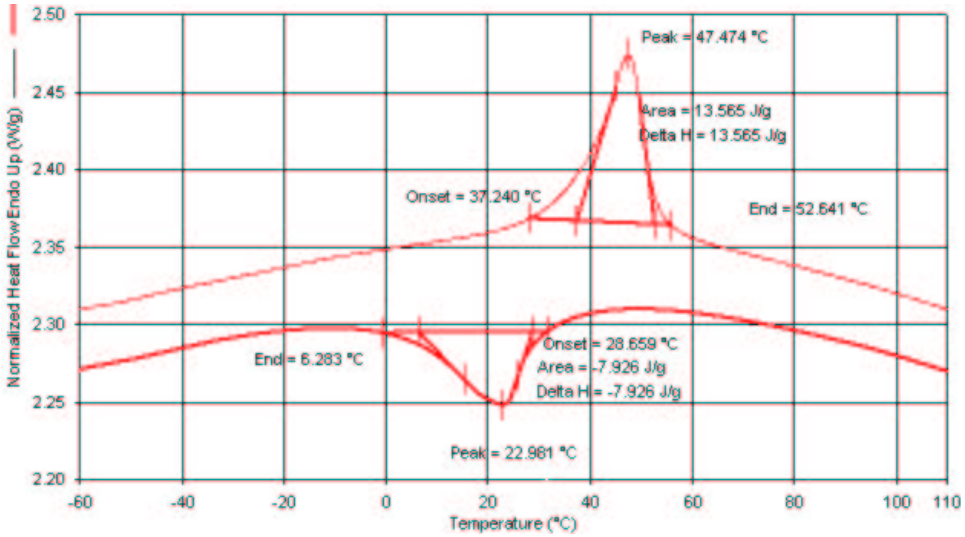

Fig. 13. Differential Scanning Calorimeter measurements of the SMA specimen.

5.3 Dynamic Results

As indicated earlier, in the Hopkinson bar experiment a 345 mm long rod instrumented with six strain gauges was placed behind the input bar. The output from these gauges is shown in Figure 15. Strain gauge number 3 ($40mm$) suffered a partial debond during the test and hence the results from this gauge are not meaningful beyond the point marked by the dark dot in the figure. The elastic wave in the input bar was not recorded due to an error in the device; all other gauges worked well and recorded the strain profile as the wave propagated down the length of the SMA rod. An x-t diagram corresponding

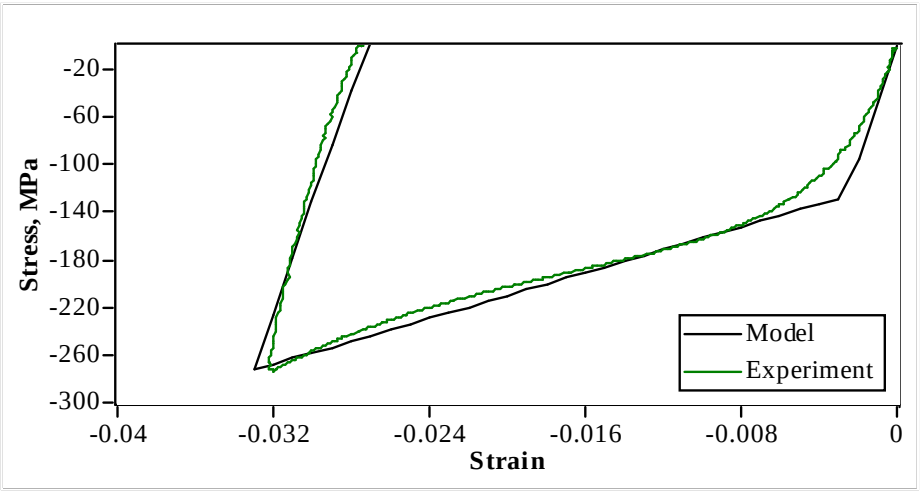

Fig. 14. Quasi-static hysteresis of SMA specimen and simulation by polynomial model.

to elastic wave propagation in this specimen is shown in Figure 16. The strain gauge locations are indicated by the thin vertical lines and the leading edge of the initial loading pulse is shown by the dark line; this pulse reaches each one of the gauges at the time where the dark line intersects the vertical lines. From the timing of the elastic wave arrival at each gauge, the elastic wave speed was determined to be 2500 m/s. The elastic wave reaches the far end of the specimen about 138 μs after impact. The duration of the loading pulse is about 90 μs; and hence an unloading pulse propagates from down the specimen with the elastic wave speed (since the unloading is elastic); this wave is shown by the line with an arrow at the tip. Time zero corresponds to the first arrival of the loading pulse at the strain gauge in the input bar.

As seen in Figure 15, the strain in the first two gauges increases rapidly to a level of about 1.3% and levels off as the load from the input bar levelled off. The oscillations seen in these gauges near the plateau are Pochhammer-Chree oscillations that appear in bars. At around 290 μs the unloading wave from the end of the loading pulse reaches the first two gauges and the strain begins to decrease; however, because the strains beyond 0.3% were the result of detwinning (see the quasi-static results in Figure 14), these strains are not recovered and a permanent strain of about 1% is left at these locations. The signal in gauge 4 clearly indicates the dispersion of the wave - higher strain levels propagate at significantly slower speeds and arrive later at the gauge location. Hence a broadening of the strain pulse can be seen - the peak in the strain at gauge 4 occurs 75 μs after elastic wave arrival while it occurs in about 20 μs in gauge 1. This delay also results in the peak strain not being sustained for too long as the elastic unloading pulse reaches the gauge quickly; once again a residual strain of peak strain - 0.3% is left at this gauge location. The same behavior is seen in gauge 5 where due to its distance from the impact end, and due to the slowness of the inelastic waves, the peak strain reached is

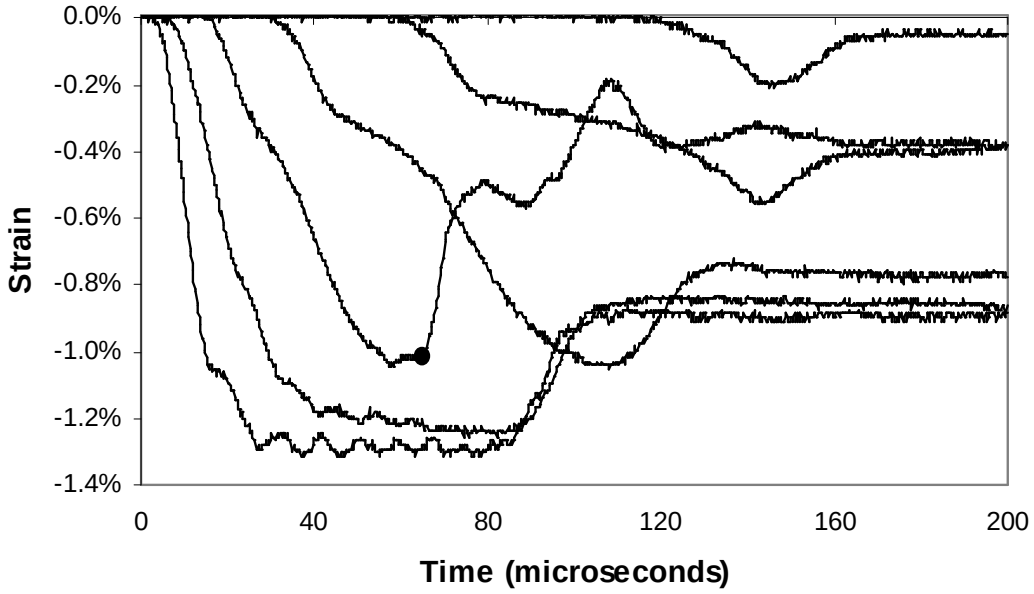

Fig. 15. Strains measured by the gauges mounted on the SMA bar. Gauge 3 suffered a partial debond at the point indicated by the dark circle and hence the data beyond this time should not be interpreted.

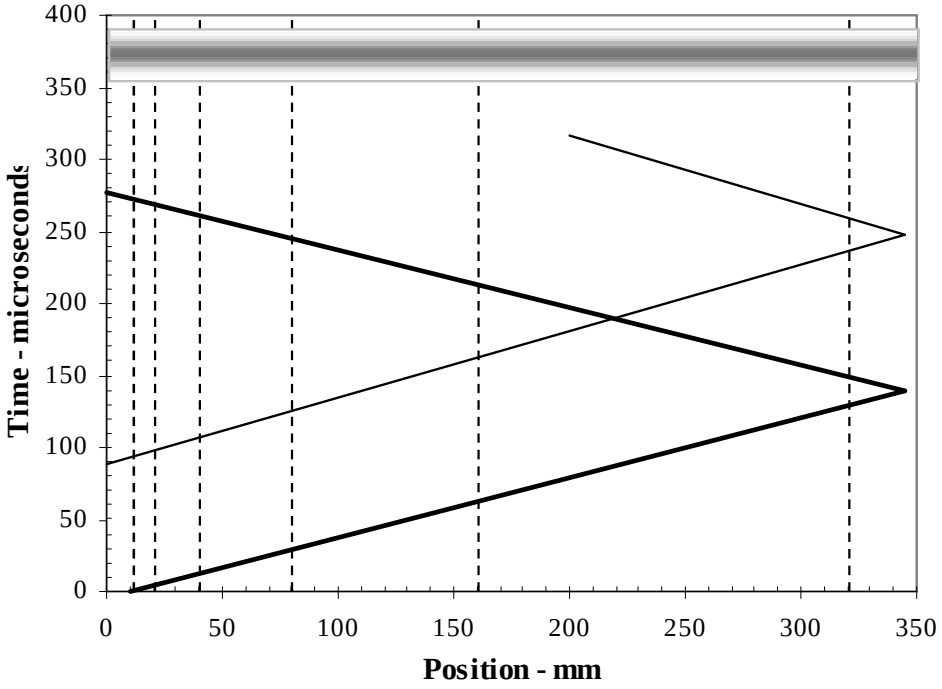

Fig. 16. X-t diagram indicating arrival of the elastic wave front at the gauge locations.

only about 0.5%; once again a residual strain is left in this location. In gauge 6, the reflected wave from the end of the SMA rod (left free in this experiment)

causes unloading of the gauge; a very small, but measurable permanent strain or detwinning is observed in this location. Subsequent to the test, the rod was heat treated through a temperature cycle taking it above A^{of} first, holding for 1 hour and then cooling below M^{of} and warming back to room temperature. All strain gauges recovered their original state indicating full recovery of the specimen.

The results of this experiment can be used to extract the dynamic stress-strain response by applying the theory of one-dimensional wave propagation in plastic rods due to (Rakhmatulin, 1945; Von Karman and Duwez, 1950; Taylor, 1958). The idea is a simple extension of the rod theory for elastic waves. Let us assume that stress is only a function of strain, i.r. $\sigma = \sigma(\varepsilon)$. Then we can rewrite equation 1 in the form

$$u_{tt} = \frac{\sigma'(\varepsilon)}{\rho} u_{xx} \tag{51}$$

Note that this is not an incremental theory, but a total strain theory; therefore unloading cannot be considered here. The wave speed $C(\varepsilon)$ of disturbances is no longer a constant as in the linear elastic case, but a function of the stress or strain:

$$C(\varepsilon) = \sqrt{\frac{\sigma'(\varepsilon)}{\rho}} \tag{52}$$

The main result of this one dimensional theory is that a given strain (or stress) level will propagate into the rod with a characteristic speed given by equation 52. If the propagation speed of stress waves in a one-dimensional rod is known (measured with strain gauges as in the experiment discussed above), equation 52 can be inverted to determine the stress-strain behavior of the material:

$$\sigma(\varepsilon) = \int_0^{\varepsilon} \sigma'(\zeta) d\zeta = \rho \int_0^{\varepsilon} C^2(\zeta) d\zeta \tag{53}$$

This representation of the wave speed is used to extract the constitutive behavior of the material (Bell, 1960; Kolsky and Douch, 1962). There exists a critical point in the stress-strain curve: $\sigma'(\varepsilon) = 0$. Strain amplitudes larger than this cannot propagate through the material. Of course, in the experiment discussed above, we have not reached this stage; in fact, this would be of interest in determining the propagation of phase transformation fronts and such experiments are in progress.

The propagation speeds of different strain levels were obtained from the results shown in Figure 15. The time of arrival of different strain levels at each

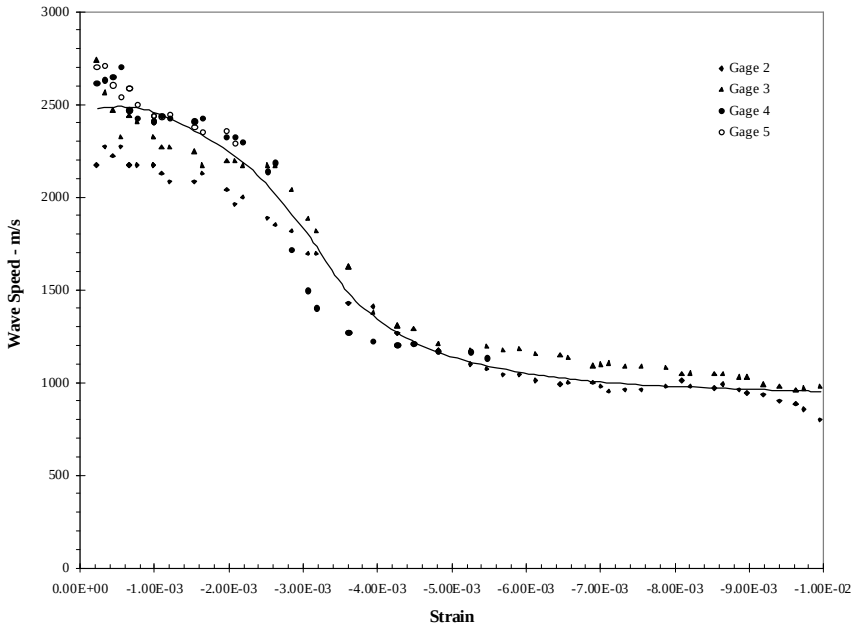

Fig. 17. Variation of the wave speed with the strain level as determined from the strain measurements. The line is an eyeball fit to indicate the data trend. Cubic fits over short segments were used to determine the wave speed corresponding to each strain level in the determination of the stress-strain behavior.

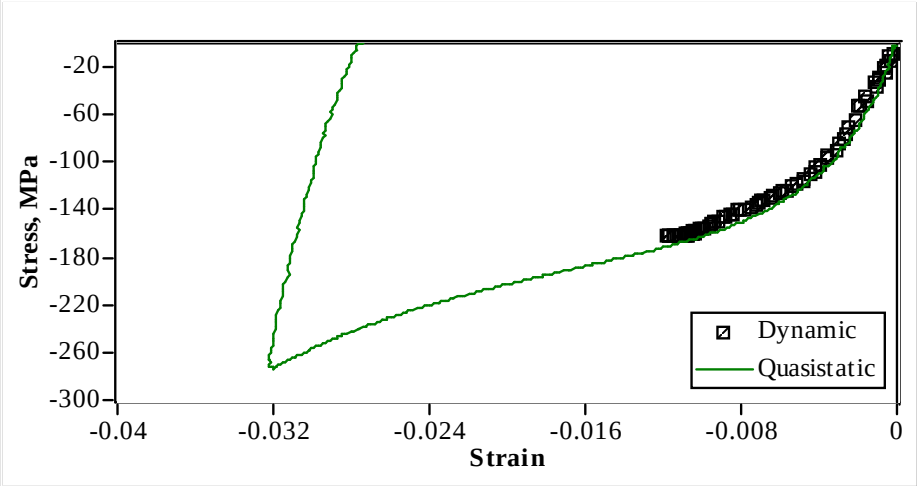

Fig. 18. Stress-strain response evaluated from one-dimensional wave propagation measurements (scatter plot) and quasi-static data (solid line).

one of the five gauges were determined from the strain measurements; the speed of each strain level $C(\varepsilon)$ was then determined from the known distances between the gauges. The variation of the wave speed with strain level is shown in Figure 17; a smooth trendline is also shown in the figure. The elastic wave speed is about 2500 m/s and all strain levels below about 0.1% travel with this speed; this suggests that there is really no significant elastic region and that even small strain levels are susceptible to dispersion. A large change in

the wave speed occurs at around 0.3% strain; this corresponds to the onset of massive detwinning deformation. Beyond this level, the wave speed drops to about 1000 m/s and varies more slowly. If the averaged data on the wave speed variation with strain level is used in equation 53, the resulting numerical integration provides the stress strain relationship associated with the detwinning deformation in the SMA rod. Such a relationship is shown in Figure 18. The scatter in the plot is a result of the averaging of the noisy data in Figure 5.e; the solid line shows the trend of the data.

5.4 Calibration of the model

The Hopkinson bar experiment was done at room temperature and due to the heat treatment of the specimen it was in fully twinned martensitic state. As polynomial model was not designed to model the phenomenon of detwinning we had to modify some of the parameters in Table 3 in order to obtain the correct prediction shown on Figure 14.

The necessary modifications included lowering the martensitic start and finish temperatures M^{os} and M^{of} by 20 $^{\circ}C$. The effect of this change affects the way the model sees the transformation surfaces on the phase diagram. At room temperature the transformation lines for martensitic start and finish deviate significantly from the almost straight-line approximation of the model and become in effect parallel to the Temperature axis. If the test temperature is known in advance, a correct shift in the M^{os} and Mf will cause the model to start and finish transforming the correct detwinning stress levels σ_s and σ_f. Taking into account that the thermal stresses are several order of magnitude less than the elastic ones and that no latent heat is generated during detwinning we effectively model the material response by an isothermal path. Figure 14 shows that the experimentally measured stress-strain response at room temperature and the predictions of the polynomial model with the above modifications taken into account are in good agreement.

6 Results and discussion

An indicated earlier, due to a trigger failure, the signal in the input bar was lost so we had only the readings of the six strain gauges on the specimen. In the numerical simulation we used the reading of the first gauge (at $10mm$) as the boundary condition and we compared the results at the remaining 5 gauges. Gauge number 3 is not included in the modelling because it got unglued during the test.

We modelled the experimental results in two different ways. First we used the polynomial SMA model with the calibration presented in Section 5.4 to predict the strains at the gauge locations. We chose the adaptive FEM scheme because of its accuracy and ability to predict precisely the positions of the both elastic and transformation shocks. Since the only phase transition was detwinning of martensite we used the isothermal solver. The results are presented on Figure 19.

As expected from the model problem studied in section 4.2 the strain wave splits into elastic and transformation front. The transformation front timing and magnitude at all strain gauges is in excellent agreement with experiment. The small wiggles observed at the first two gauges are due to surface effects caused by the impacting projectile. Such effects cannot possibly be modelled within a 1D formulation.

There is a noticeable disagreement in the timing of the elastic fronts. The reason for this is the deviations from linear behavior for small strains. The polynomial model always predicts a linear response until the beginning of phase transition. However an inspection of Figure 14 shows a more oblique cubic-like stress-strain relationship for small strain values which is at the root of the disagreement. To verify this explanation we preformed an independent numerical run with the hysteresis on Figure 14 being modelled by a sixth degree polynomial. The curve fit was made in least squares sense and the unloading is assumed linear with the modulus of elasticity of martensite as measured by the quasi-static experiments. The results are shown on Figure 20. This time the wave profiles are matched much more closely and the small disagreements can be attributed to measurement errors and effects of lateral inertia not included in the simulation.

Two things should be noted about this curve fit. First, unlike a constitutive model based on physical principles such an approach will only work for a particular SMA material and particular operating temperature. Secondly, due to the fact that the transformation is mostly detwinning of martensite there is no significant release of latent heat, so the quasi-static isothermal hysteresis can be assumed very close to the adiabatic one.

7 Conclusions

We explored several different methods for the numerical treatment of the impact loading problem. Both explicit FD schemes and FEM methods were able to accurately reproduce a known analytical solution to the Riemann problem. The FD scheme considered are fast and easy to implement and the solution captures the main characteristics of the wave profile. However the scheme pro-

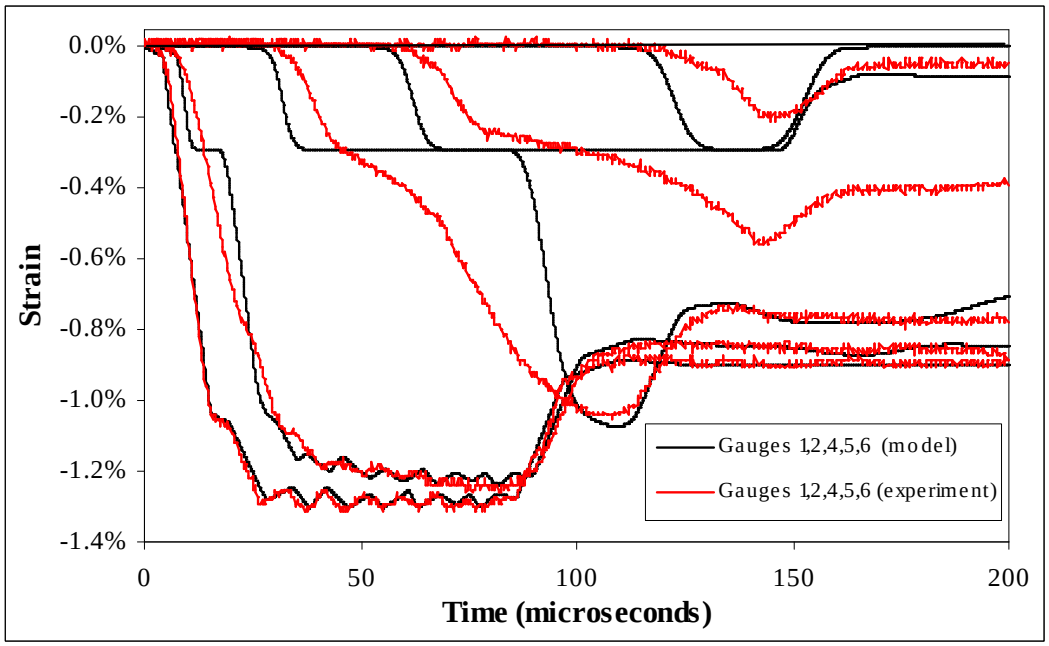

Fig. 19. And adaptive FE analysis of experimental data under isothermal conditions. The first strain gauge is used to define the boundary condition.

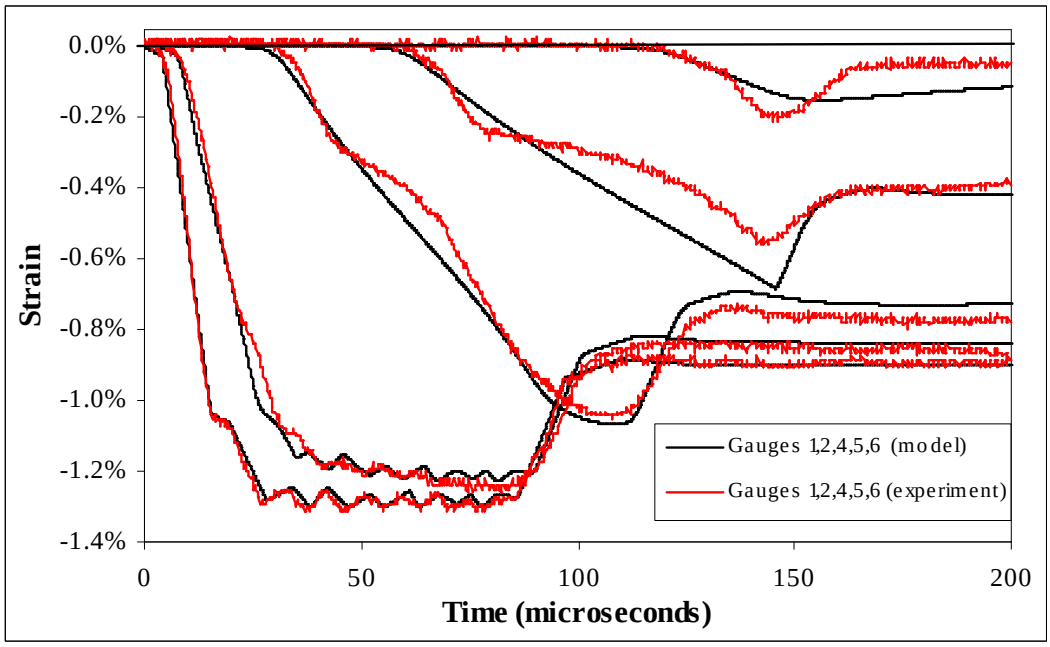

Fig. 20. And adaptive FE analysis of experimental data under isothermal conditions and a curvefit of the hysteresis. The first strain gauge is used to define the boundary condition.

duces large amounts of numerical dissipation which lead to overly smoothed solutions. This drawback can be mitigated by careful selection of the spatial and time discretization.

As a whole the FEM methods showed a definite advantage in precision and

accuracy over FD schemes. The solutions coincide completely with the analytical solution with a subsonic shock described in (Bekker, 2001). Further, their main disadvantage - slow implicit time integration - can be successfully overcome by using adaptive techniques. The use of mesh adaptivity also greatly increases the robustness of the scheme.

On the experimental side, it has been shown that an instrumented Hopkinson bar can be used effectively to evaluate the wave and phase propagation characteristics in the SMA rods. Through the use of multiple strain gages, the phase velocity at the different strain levels was obtained easily; a deformation theory of plasticity approach was used to interpret the dispersion in terms of the underlying dynamic material response of the material. The material and environmental conditions used in these experiments correspond to a detwinning deformation of the martensitic phase, but the methods can be easily adapted to stress induced martensitic transformation in tests at higher temperatures.

Through careful calibration of the polynomial SMA model we were also able to predict accurately the peak stress levels when compared with experimental results. A much better predictions however are obtained by curve fitting the experimental hysteresis. The main drawback of the polynomial SMA model is its initial linear response and the existence of kinks on the hysteresis curve. Further work is required to improve the model and capture more closely the detwinning phenomenon. We would also like to point out the need to develop analytical solutions to more complicated initial-boundary value problems with the type of nonlinearities introduced by the SMAs.

Finally, we would like to point out the excellent energy dissipation capabilities of SMA rods. The model study in Section 4.2 suggests that SMAs can be used in a very effective manner as damping and shock-absorption devices. The work can be extended to include more complicated 2- and 3-D geometries which will give true understanding of their potential in that area.

Acknowledgements

The authors would like to acknowledge the financial support of the Air Force Office of Scientific Research, Grant No. F49620-01-1-0196 monitored by Dr. Dan Segalman as well as the Office of Naval research Grant No. M00014-99-1-1069 monitored by Dr. Roshdy Barsoum.

References

Abeyaratne, R., Kim, S.-J., Knowles, J. K., 1993. One-dimensional continuum model for shape memory alloys. Int. J. Solids Struct. 41, 541–571.

Abeyaratne, R., Kim, S.-J., Knowles, J. K., 1994. Continuum Modeling of Shape Memory Alloys. New York, pp. 59–69.

Abeyaratne, R., Knowles, J. K., 1991. Kinetic relations and the propagation of phase boundaries in solids. Arch. Rational Mech. Anal. 114 (2), 119–154.

Abeyaratne, R., Knowles, J. K., 1993. Continuum model of a thermoelastic solid capable of undergoing phase transformation. J. Mech. Phys. Solids 41, 541–571.

Abeyaratne, R., Knowles, J. K., 1994a. Dynamics of propagating phase boundaries: adiabatic theory for thermoelastic solids. Physica D (79), 269–288.

Abeyaratne, R., Knowles, J. K., 1994b. Dynamics of propagating phase boundaries: Thermoelastic solids with heat conduction. Archive for Rational Mechanics and Analysis 126 (3), 203–230.

Abeyaratne, R., Knowles, J. K., 1997. Impact-induced phase transitions in thermoelastic solids. Phil. Trans. R. Soc. Lond. A (355), 843–867.

Bekker, A., Jimenez-Victory, J., Popov, P., Lagoudas, D., 2002. Impact induced propagation of phase transformation in a shape memory alloy rod. International Journal of Plasticity accepted for publication.

Bekker, A., J.-V. J. L. D., December 2001. Shock propagation of phase transitions in shape memory alloy rods. Tech. rep., Center for Mechanics of Composites, Texas A&M University.

Bell, J., 1960. Propagation of large amplitude waves in annealed aluminum. Journal of Applied Physics 31, 227–282.

Bell, J., 1962. Experimental study of dynamic plasticity at elevated temperatures. Experimental Mechanics 2, 1–6.

Birman, V., 1996. Review of constitutive equations for shape memory alloys. In: Li, Y. K., Su, T. C. (Eds.), Proc. of 11th ASCE Conf. on Engineering Mechanics. Vol. 2. ASCE, New York, pp. 792–795.

Bo, Z., Lagoudas, D. C., 1999a. Thermomechanical modeling of polycrystalline SMAs under cyclic loading, part I: theoretical derivations. International Journal of Engineering Science 37, 1089–1140.

Bo, Z., Lagoudas, D. C., 1999b. Thermomechanical modeling of polycrystalline SMAs under cyclic loading, part I: theoretical derivations. International Journal of Engineering Science 37.

Bo, Z., Lagoudas, D. C., 1999c. Thermomechanical modeling of polycrystalline SMAs under cyclic loading, part III: evolution of plastic strains and two-way shape memory effect. International Journal of Engineering Science 37, 1175–1203.

Bo, Z., Lagoudas, D. C., 1999d. Thermomechanical modeling of polycrystalline SMAs under cyclic loading, part IV: modeling of minor hysteresis loops. International Journal of Engineering Science 37, 1205–1249.

Bodner, S., Clifton, J., 1967. An experimental investigation of elastic-plastic

pulse propagation in aluminum rods. Journal of Applied Mechanics 34 (1), 91–99.

Boyd, J. G., Lagoudas, D. C., 1994. Thermomechanical response of shape memory composites. Journal of Intelligent Material Systems and Structures 5, 333–346.

Boyd, J. G., Lagoudas, D. C., 1996. A thermodynamic constitutive model for the shape memory materials. Part I. The monolithic shape memory alloys. Int. J. Plasticity 12 (6), 805–842.

Brinson, L. C., 1993. One-dimensional constitutive behavior of shape memory alloys: Thermomechanical derivation with non-constant material functions and redefined martensite internal variable. J. of Intell. Mater. Syst. and Struct. 4, 229–242.

Brinson, L. C., Lammering, R., 1993. Finite element analysis of the behavior of shape memory alloys and their applications. International Journal of Solids and Structures 30 (23), 3261–3280.

Chen, Y.-C., Lagoudas, D. C., 2000. Impact induced phase transformation in shape memory alloys. J. Mech. Phys. Solids 48 (2), 275–300.

Chiddister, J., Malvern, L., 1963. Compression-impact testing of aluminum at elevated temperatures. Experimental Mechanics 3 (81-90).

Clifton, R., Bodner, S., Jun. 1966. An analysis of longitudinal elastic-plastic pulse propagation. Transactions of the ASME 33, 248–255.

Cory, J.S., M.-J., 1985. Nonequilibrium thermostatics. J. Appl. Phys. 58, 3282–3294.

Escobar, J., Clifton, R., 1993. Pressure-shear impact induced phase transformation in cu-14.44al-4.19ni single crystals. J. Mater. Sci. Engng A (170), 125–142.

Feng, Z. C., Li, D. Z., July 1996. Dynamics of a mechanical system with a shape memory alloy bar. Journal of Intelligent Material Systems and Structures 7 (4), 399–410.

Fosdick, R., Ketema, Y., 1998. Shape memory alloys for passive vibration damping. Journal of Intelligent Systems and Structures 9, 854–870.

Funakubo, H., 1987. Shape Memory Alloys. Gordon and Bleach, New York.

Godlewsky, E., Raviart, P., 1996. Numerical Approximation of Hyperbolic Systems of Conservation Laws. Applied Mathematical Sciences. Springer-Verlag, New York.

Graesser, E. J., November 1995. Effect of intrinsic damping on vibration transmissibility of nickel-titanium shape memory alloy springs. Metallurgical and Materials Transactions A 26A, 2791–2796.

Graff, K., 1975. Wave Motion in Elastic Solids. Oxford University Press, London.

Jimenez-Vicktory, J. C., December 1999. Dynamic analysis of impact induced phase transformation in shape memory alloys using numerical techniques. Aerospace engineering, Texas A&M University.

Kolsky, H., 1949. An investigation of the mechanical properties of materials at very high rates of loading. Proc. R. Soc. Lond. B 62, 676–700.

Kolsky, H., 1963. Stress Waves in Solids. Dover Publications.

Kolsky, H., Douch, L., 1962. Experimental studies in plastic wave propagation. Journal of the Mechanics and Physics of Solids 10, 195–223.

Lagoudas, D., Bo, Z., Qidwai, M., 1996. A unified thermodynamic constitutive model for sma and finite element analysis of active metal matrix composites. Mechanics of Composite Structures 3, 153–179.

Lagoudas, D., Shu, S., 1999. Residual deformations of active structures with sma actuators. International Journal of Mechanical Sciences 41, 595–619.

Lagoudas, D. C., Khan, M. M., Mayes, J. J., 2001. Modelling of shape memory alloy springs for passive vibration isolation. In: Proceedings of IMECE01.

Liang, C., Rogers, C. A., 1990. One-dimensional thermomechanical constitutuve relations for shape memory materials. In: 31st AIAA/ASME/ASCE/AHS/ASC Structures, Structural Dynamics and Materials Conference. pp. 16–28.

Malvern, L., 1977. Introduction to the Mechanics of a Continuous Medium. Prentice-Hall Inc., Englewood Cliffs, N.J.

Mayes, J. J., Lagoudas, D. C., August 2001. An experimental investigation of shape memory alloy springs for passive vibration isolation. In: AIAA Space 2001 Conference and Exposition.

McNichols, J.L., C.-J., 1987. Thermodynamics of nitinol. J. Appl. Phys. 61, 972–984.

Nemat-Nasser, S., Isaacs, J., Starrett, J., 1991. Hopkinson techniques for dynamic recovery experiments. Proc. R. Soc. Lond. A 435, 371–391.

Newmark, N. M., 1959. A method of computation for structural dynamics. Journal of Engineering Mechanics Division, ASCE , 67–94.

Oberaigner, E., Tanaka, K., Fischer, F., 1996. Investigation of the damping behavior of a vibrating shape memory alloy rod using a micromechanical model. Smart Materials and Structures (3), 456–463.

Patoor, E., Eberhardt, A., Berveiller, M., 1996. Micromechanical modelling of superelasticity in shape memory alloys. Journal de Physique IV 6, C1–277–292.

Pence, T., 1986. On the emergence and propagation of a pahse boundary in ana elastic bar with a suddenly applied end load. J. Elasticity (16), 3–42.

Qidwai, M. A., Lagoudas, D. C., 2000. Numerical implementation of a shape memory alloy thermomechanical constitutive model using return mapping algorithms. International Journal for Numerical Methods in Engineering 47, 1123–1168.

Rakhmatulin, K. A., 1945. Propagation of an unloading wave (in russian). Prikh.Mat. Mekh. 9, 91–100.

Reddy, J. N., 1993. An Introduction to the Finite Element Method. McGraw-Hill.

Siderey, N., Patoor, E., Berveiller, M., Eberhardt, A., 1999. Constitutive equations for polycrystalline thermoelastic shape memory alloys. part i. intragranular interactions and behavior of the grain. International Journal of Solids and Structures. 36, 4289–4315.

Sun, Q. P., Hwang, K. C., 1993a. Micromechanics modeling for the constitutive behavior of polycrystalline shape memory alloys — I. Derivation of general relations. J. Mech. Phys. Solids 41 (1), 1–17.

Sun, Q. P., Hwang, K. C., 1993b. Micromechanics modelling for the constitutive behavior of polycrystalline shape memory alloys — II. Study of the individual phenomena. J. Mech. Phys. Solids 41 (1), 19–33.

Tanaka, K., 1986. A thermomechanical sketch of shape memory effect: One-dimensional tensile behavior. Res Mechanica 18, 251–263.

Taylor, G., 1958. The plastic wave in a wire extended by an impact load, The Scientific Papers of G.I. Taylor,Vol.I,. Mechanics of Solids. University Press, Cambridge.

Thomson, P., Balas, G. J., Leo, P. H., March 1995. The use of shape memory alloys for passive structural damping. Smart Materials and Structures 4 (1), 36–41.

Von Karman, T., 1942. On the propagation of plastic deformation in solids. Tech. rep., NDRC Report No. A-29, OSRD No. 365.

Von Karman, T., Duwez, P., 1950. The propagation of plastic deformation in solids. Journal of Applied Physics 21, 987–994.

Wayman, C. M., 1983. Phase transformations, nondiffusive. In: Cahn, R. W., Haasen, P. (Eds.), Physical Metallurgy. North-Holland Physics Publishing, New York, pp. 1031–1075.

Yiu, Y. C., Regelbrugge, M. E., April 1995. Shape-memory alloy isolators for vibration suppression in space applications. 36th AIAA/ASME/ASCE/AHS/ASC Structures, Structural Dynamics, and Materials Conference , 3390–3398.

Zienkiewicz, O.C., Z.-J., 1987. A simple error estimator and an adaptive procedure for practical engineering analysis. International Journal for Numerical Methods in Engineering 24, 337–357.